A&A 604, A135 (2017)
DOI: 10.1051/0004-6361/201730986

Astronomy & Astrophysics

The *Gaia*-ESO Survey: dynamics of ionized and neutral gas in the Lagoon nebula (M 8)⋆,⋆⋆

F. Damiani[1], R. Bonito[1,2], L. Prisinzano[1], T. Zwitter[3], A. Bayo[4], V. Kalari[5], F. M. Jiménez-Esteban[6], M. T. Costado[7], P. Jofré[8,9], S. Randich[10], E. Flaccomio[1], A. C. Lanzafame[11], C. Lardo[12], L. Morbidelli[10], and S. Zaggia[13]

[1] INAF – Osservatorio Astronomico di Palermo G. S. Vaiana, Piazza del Parlamento 1, 90134 Palermo, Italy
e-mail: damiani@astropa.inaf.it
[2] Dipartimento di Fisica e Chimica, Università di Palermo, Piazza del Parlamento 1, 90134 Palermo, Italy
[3] Faculty of Mathematics and Physics, University of Ljubljana, Jadranska 19, 1000 Ljubljana, Slovenia
[4] Instituto de Física y Astronomía, Universidad de Valparaíso, Chile
[5] Departamento de Astronomía, Universidad de Chile, Casilla 36-D Santiago, Chile
[6] Departamento de Astrofísica, Centro de Astrobiología (INTA-CSIC), ESAC Campus, Camino Bajo del Castillo s/n, 28692 Villanueva de la Cañada, Madrid, Spain
[7] Instituto de Astrofísica de Andalucía-CSIC, Apdo. 3004, 18080 Granada, Spain
[8] Institute of Astronomy, University of Cambridge, Madingley Road, Cambridge CB3 0HA, UK
[9] Núcleo de Astronomía, Facultad de Ingeniería, Universidad Diego Portales, Av. Ejército 441, Santiago, Chile
[10] INAF – Osservatorio Astrofisico di Arcetri, Largo E. Fermi 5, 50125 Florence, Italy
[11] Dipartimento di Fisica e Astronomia, Sezione Astrofisica, Università di Catania, via S. Sofia 78, 95123 Catania, Italy
[12] Laboratoire d'Astrophysique, École Polytechnique Fédérale de Lausanne (EPFL), Observatoire de Sauverny, 1290 Versoix, Switzerland
[13] INAF – Padova Observatory, Vicolo dell'Osservatorio 5, 35122 Padova, Italy

Received 13 April 2017 / Accepted 23 May 2017

ABSTRACT

Aims. We present a spectroscopic study of the dynamics of the ionized and neutral gas throughout the Lagoon nebula (M 8), using VLT-FLAMES data from the *Gaia*-ESO Survey. The new data permit exploration of the physical connections between the nebular gas and the stellar population of the associated star cluster NGC 6530.
Methods. We characterized through spectral fitting emission lines of Hα, [N II] and [S II] doublets, [O III], and absorption lines of sodium D doublet, using data from the FLAMES-Giraffe and UVES spectrographs, on more than 1000 sightlines toward the entire face of the Lagoon nebula. Gas temperatures are derived from line-width comparisons, densities from the [S II] doublet ratio, and ionization parameter from Hα/[N II] ratio. Although doubly-peaked emission profiles are rarely found, line asymmetries often imply multiple velocity components along the same line of sight. This is especially true for the sodium absorption, and for the [O III] lines.
Results. Spatial maps for density and ionization are derived, and compared to other known properties of the nebula and of its massive stars 9 Sgr, Herschel 36 and HD 165052 which are confirmed to provide most of the ionizing flux. The detailed velocity fields across the nebula show several expanding shells, related to the cluster NGC 6530, the O stars 9 Sgr and Herschel 36, and the massive protostar M 8East-IR. The origins of kinematical expansion and ionization of the NGC 6530 shell appear to be different. We are able to put constrains on the line-of-sight (relative or absolute) distances between some of these objects and the molecular cloud. The data show that the large obscuring band running through the middle of the nebula is being compressed by both sides, which might explain its enhanced density. We also find an unexplained large-scale velocity gradient across the entire nebula. At larger distances, the transition from ionized to neutral gas is studied using the sodium lines.

Key words. ISM: individual objects: Lagoon nebula – ISM: general – HII regions

1. Introduction

The Lagoon nebula (M 8, NGC 6523) is one of the brightest H_{II} regions in the solar neighborhood, and has been the subject of many observational studies (e.g., Lada et al. 1976, in CO and optical lines; Tothill et al. 2002, in CO and sub-mm; Takeuchi et al. 2010, in CO). It harbors the young cluster NGC 6530, only a few Myrs old, and also intensively studied especially in recent years at optical, infrared and X-ray wavelengths (e.g., Walker 1957; van den Ancker et al. 1997; Sung et al. 2000; Damiani et al. 2004, 2006; Prisinzano et al. 2005, 2007; Kumar & Anandarao 2010; Povich et al. 2013). The H_{II} region is illuminated by many massive stars of O and B spectral types, the hottest one being 9 Sgr (HD 164794, type O4V((f))z); a few other late-O or B type stars are also found in the region. The optically brightest part of the Lagoon nebula is the so-called Hourglass nebula, which surrounds and partially oscures the O7:V star Herschel 36 (Woodward et al. 1986); stars in the Hourglass are thought to be younger than the NGC 6530 cluster. Also noteworthy is the presence, to the east of NGC 6530, of

⋆ Based on observations collected with the FLAMES spectrograph at VLT/UT2 telescope (Paranal Observatory, ESO, Chile), for the *Gaia*-ESO Large Public Survey (program 188.B-3002).
⋆⋆ Full Tables A.1 and A.2 are only available at the CDS via anonymous ftp to cdsarc.u-strasbg.fr (130.79.128.5) or via http://cdsarc.u-strasbg.fr/viz-bin/qcat?J/A+A/604/A135

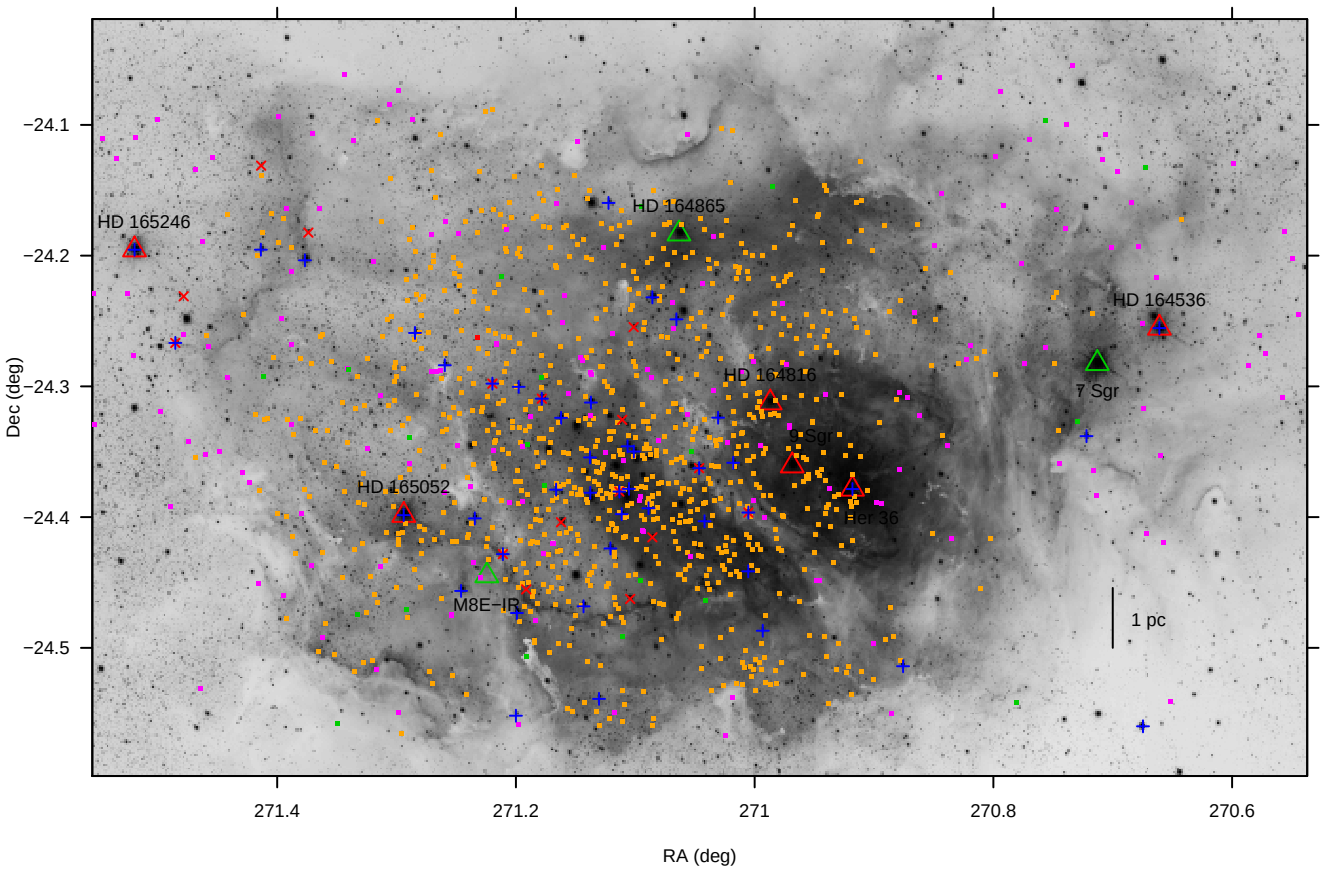

Fig. 1. VPHAS+ image of the Lagoon nebula (size 55.8′ × 34.8′, corresponding to 20.36 × 12.7 pc), with superimposed all *Gaia*-ESO target positions used in this work. Giraffe targets are indicated with magenta (sky fibres) or orange (faint stars) filled squares. UVES sky fibres are indicated with red (setup 580) or green (setup 520) filled squares. Only one UVES-580 sky fibre position is not coincident with (and its symbol not hidden by) an UVES-520 sky fibre position. UVES stars are indicated with red crosses (setup 580) or blue "+" signs (setup 520). Red triangles indicate the O stars HD 165246, HD 165052, HD 164816, 9 Sgr, Herschel 36, and HD 164536. Green triangles indicate the massive objects M 8E-IR, HD 164865, and 7 Sgr. North is up and east to the left.

the embedded massive protostar M 8E-IR (Wright et al. 1977; Simon et al. 1984; Henning & Gürtler 1986), indicating that star formation in the region has also taken place recently. The most recent determination of the distance of the NGC 6530 cluster (and by inference of the H_{II} region as well) is 1250 pc (Prisinzano et al. 2005). The properties of the whole region were reviewed by Tothill et al. (2008).

The Lagoon nebula and its stellar population show a well-defined spatial organization. The brightest nebular region (Hourglass) does not lie near the geometrical center of the whole nebula, but several arcmin (~2 pc) to the west. Closer to the nebula center lies instead the bulk of low-mass cluster stars (Damiani et al. 2004), cospatial with the B stars. The most massive member 9 Sgr is also offset with respect to the B stars, but appears not directly related to any localized bright nebulosity, leading Lada et al. (1976) to suggest that it actually lies several parsecs in front of the nebula, not within it. All around the central region, many bright-rimmed dark clouds are found, which being located along the outer border of the nebula suggest the blister nature of the H_{II} region. Behind one of them to the south-east of the main cluster, the mentioned young, massive star M 8E-IR is found. This and other low-mass stars in the same neighborhood show indications of being younger than the main NGC 6530 cluster (Damiani et al. 2004). The bright Hourglass region has received much more attention than the outer nebula parts, which remain relatively little studied.

In this work we studied the kinematics of the ionized and neutral gas giving rise to the strong optical emission lines (Hα, [N II], [S II], [O III]), and sodium D absorption lines, across the whole nebula, using new spectroscopic data from the *Gaia*-ESO Survey (Gilmore et al. 2012; Randich et al. 2013). In Sect. 2 we describe the observations, while in Sect. 3 we present our results. In Sect. 4 we discuss the main implications of our work for the structure and dynamics of the Lagoon nebula, including issues that deserve further research.

2. Observational data

The observations of the Lagoon nebula were obtained as part of the *Gaia*-ESO Survey (internal release *iDR4*), targeting Milky Way stars and clusters across a wide range of parameters with the ESO VLT-FLAMES multi-fibre spectrograph (Pasquini et al. 2002). Twenty-seven observing blocks (OBs) were devoted to NGC 6530 as part of the Survey program, down to a limiting stellar magnitude $V = 19$. Observations were spread over 17 nights, in September 2012 and June–September 2013. Fifteen fibres per OB were targeted at star-free sky positions, interspersed between stellar position, with the intent of obtaining purely nebular spectra needed to correct the stellar spectra through subtraction. Spectrographs used were Giraffe (setup HR15N, $R \sim 19\,000$, wavelength range 6444–6818 Å) and UVES (setup 580, $R \sim 47\,000$, range 4768–6830 Å; and setup 520, $R \sim 47\,000$, range

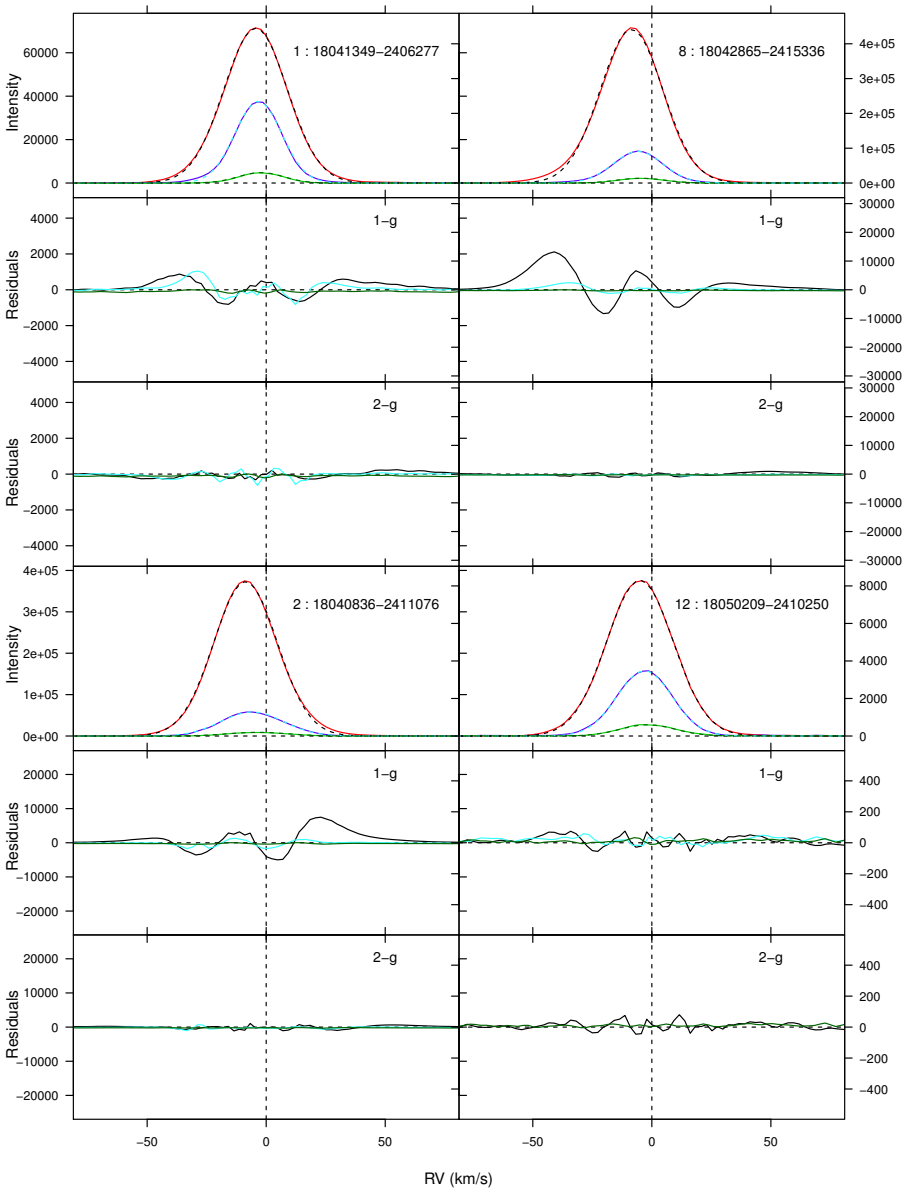

Fig. 2. Four examples of nebular line profiles of Hα (red), [N II] 6584 (blue), and [S II] 6731 (green) lines, and their best-fit models using both one- and two-Gaussian models (black, cyan and dark-green dashed lines, for Hα, [N II] and [S II] respectively). The ordinate scale is the same for all lines. Only pure-sky spectra from Giraffe are shown. *Each panel labeled with sky position* shows the observed spectrum with superimposed the one-Gaussian best-fit model for each line. Below it, the fit residuals (labeled "1-g") for the one-Gaussian model are shown, with an ordinate scale enlarged 15 times; still below, the fit residuals for the two-Gaussian model (labeled "2-g") are shown on the same scale.

4180–6212 Å). The number of sky spectra obtained with Giraffe is 647 (on 197 individual sky positions), four spectra with UVES setup 580 (three positions), and 25 spectra with UVES setup 520 (21 positions). In addition, being so bright, the nebula dominates clearly the stellar spectra of faint stars, and the strongest nebular lines could be studied with good results whenever the ratio between Hα peak and stellar continuum is larger than 100 (henceforth "faint stars"), so that the Hα line cannot be dominated by the star, even in strongly accreting T Tauri stars. The same method was successfully used by us in a previous work on the emission of the Carina nebula using *Gaia*-ESO data (Damiani et al. 2016). The number of faint star spectra in the NGC 6530 *Gaia*-ESO dataset is 980 (892 individual stars, with some having been observed more than once). Therefore, only considering Giraffe spectra, we have nebular spectra for 1089 positions across the Lagoon nebula. The Giraffe HR15N wavelength range includes several strong nebular lines: Hα, the neighboring [N II] lines at 6548, 6584 Å, and the two [S II] lines at 6716, 6731 Å. Also the He I line at 6678 Å falls in the range, but is found to be too weak in our spectra for a proper study. Spectra for the same sky position were coadded to improve the S/N ratio. All the studied nebular lines are orders of magnitude stronger than atmospheric lines, as estimated from other *Gaia*-ESO spectra in clusters free of nebulosity.

The UVES sky spectra are very few as mentioned, and add little information despite the much wider wavelength range; they are therefore not considered further. On the other hand, the UVES spectra of stellar targets in NGC 6530 are more numerous (16 stars using setup 580, and 44 using setup 520, mostly of early type), and were used to study two important lines: the [O III] line at 5007 Å, clearly detected in most spectra, and the Na I D1, D2 absorption lines at 5895.92, 5889.95 Å. The latter enabled us to perform a comparative study of the ionized and the neutral gas in the region. Like the ionic lines, also these sodium absorption lines are much stronger than typical atmospheric sodium absorption. An Hα image of the Lagoon nebula from the VPHAS+ survey (Drew et al. 2014) is shown in Fig. 1, together with all sky positions considered here, and positions of several of the most massive stars.

Since the exposure times (20–50 min) were determined by the requirements dictated by the faintest stars, the signal-to-noise ratio (S/N) in the main nebular lines is usually very high (but

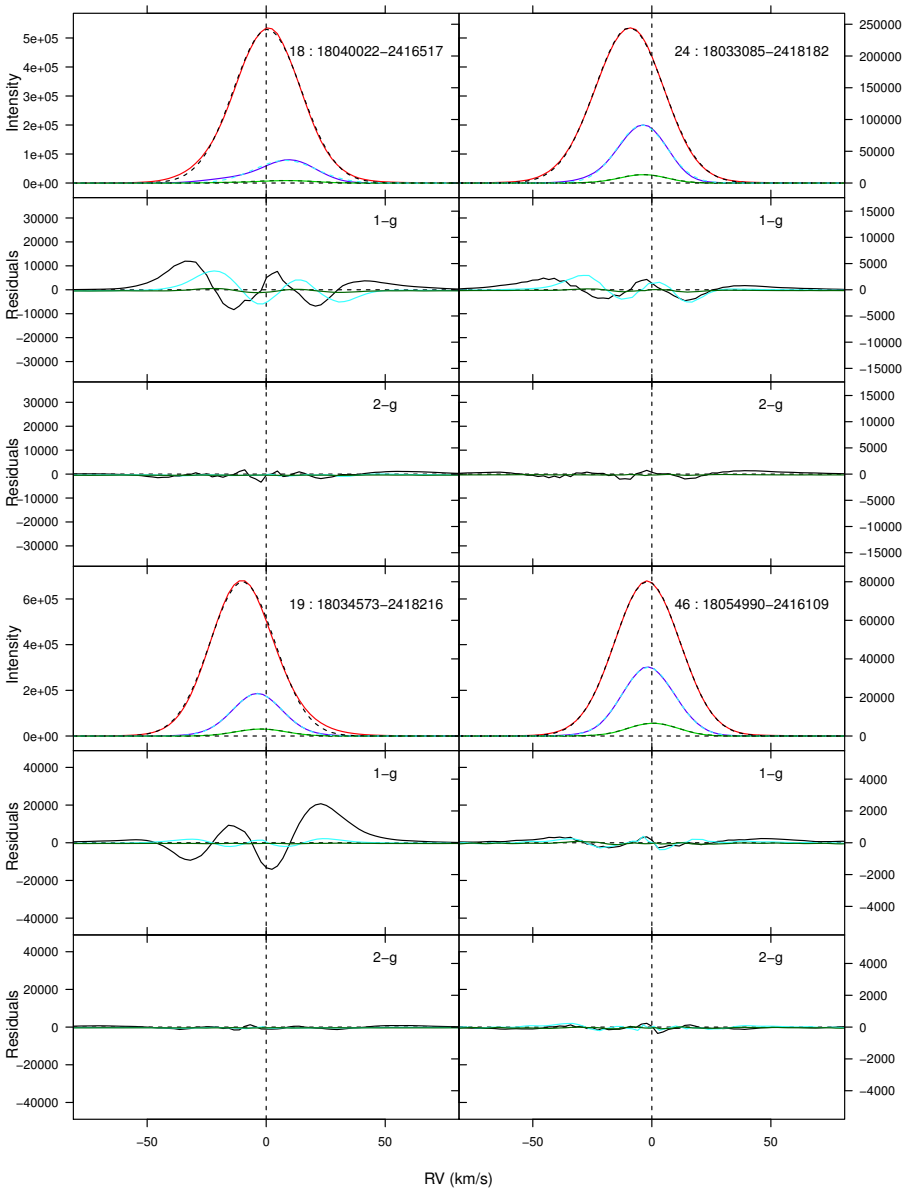

Fig. 3. Additional examples of observed line profiles and their best-fit models, as in Fig. 2, showing large differences between the peak radial velocities of Hα and [N II], and occasional asymmetrical residuals.

lines remain unsaturated). The high S/N and the large number of nebular positions comprised in our dataset make it one of the richest datasets ever available for the study being performed.

3. Results

3.1. Hα, [N II] and [S II] lines from Giraffe data

In order to study the dynamics of the nebular gas the optical emission lines were analyzed and modeled with analytical functions, starting with lines from Giraffe spectra. Figures 2 to 4 show several examples of the observed lines of Hα, [N II] 6584 Å, and [S II] 6731 Å (panels labeled with coordinates), and the residuals after subtraction of single-Gaussian (panels labeled with 1-g) or double-Gaussian (labeled 2-g) best-fit models. In nearly all cases the optical lines were found single-peaked: among all 197 pure-sky fibres only two cases of doubly-peaked lines were found (Fig. 4, right panels), and only in the [N II] and [S II] lines while not in Hα. In general, lines were found to be nearly Gaussian in shape, suggesting a single kinematical component along each line of sight for each emitting ion, as the representative examples of Figs. 2 and 3 show. However, while a single Gaussian (henceforth 1-g model) accounted well for the bulk of the emission in each line, examination of the fitting residuals (panels labeled 1-g) revealed that the detailed line shape was systematically misreproduced by a simple Gaussian function, by a small but significant amount in terms of the available S/N (we note that the ordinate scale in each of the 1-g residuals panels is 1/15 that of the panel above it). The systematic pattern of the 1-g model residuals was suggestive of at least two unresolved velocity components along the same sight-line; only in rare cases the 1-g residuals showed no such pattern (Fig. 2, spectrum #12). In order to model the line profiles in detail, double-Gaussian (2-g) models were therefore attempted, whose residuals are also shown in Figs. 2–4 (panels labeled 2-g): these showed in nearly all cases no systematic patterns, indicating that two Gaussian components provide a sufficient characterization of emission lines in the Lagoon nebula. It should be remarked that each emission line (Hα, [N II] 6584 and [S II] 6717, 6731 Å) was fit independently; as the first three panels of Fig. 3 show particularly well, the Hα emission peak may lie at velocities significantly different than the peaks of [N II] and

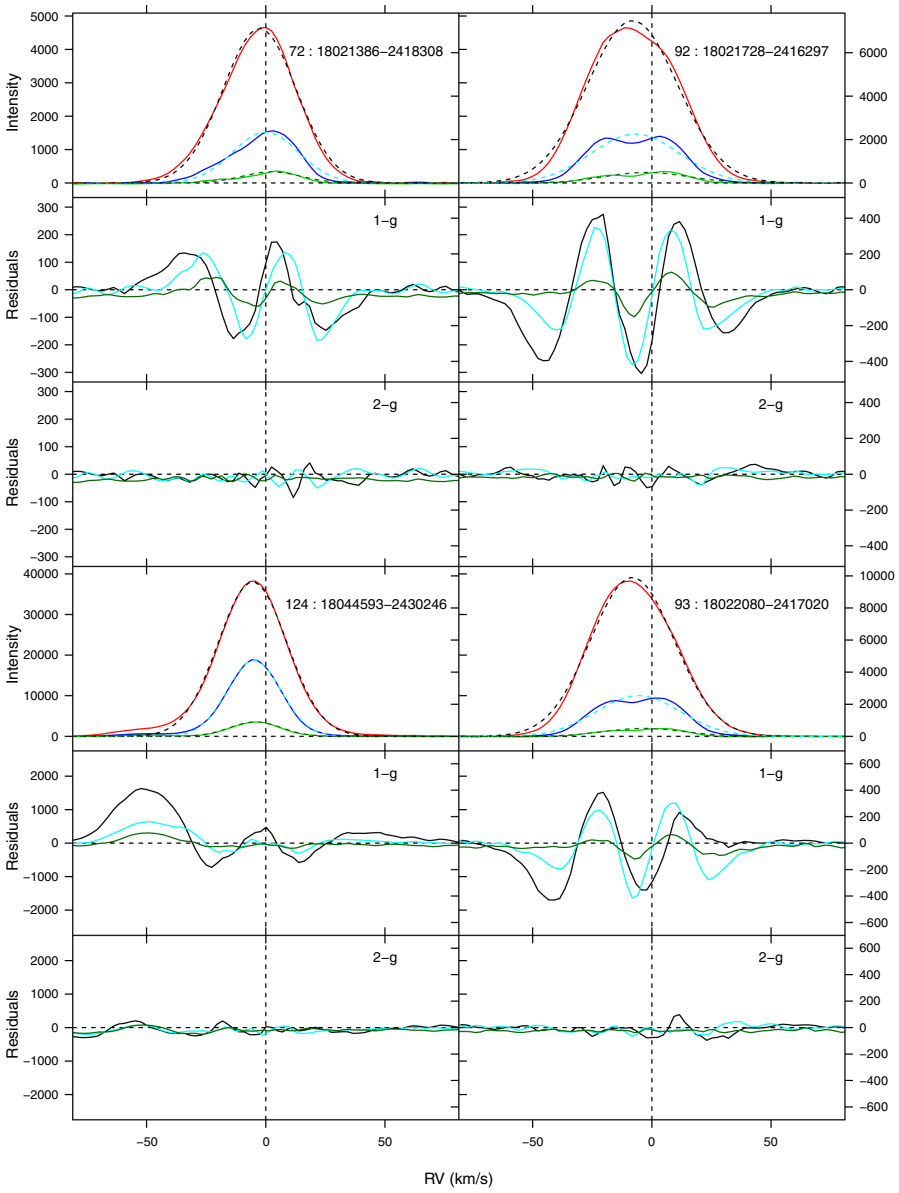

Fig. 4. Additional examples of observed line profiles and their best-fit models, as in Fig. 2. Here we show line profiles with the most evident distortions, even showing double peaks in [N II] (*right panels*).

[S II] lines. All velocities here are heliocentric. Results from our 1-g best fits are reported in Table A.1.

While the 2-g models can be considered in some sense better than the 1-g ones because of the smaller residuals, the corresponding best-fit parameters must be treated with caution. The blue and red best-fit radial velocities (RVs) of each modeled line were in most cases only a few km s^{-1} from one another, that is much closer together than the line widths (σ) themselves: this makes the relative intensities of the two Gaussian components much more uncertain than their total value, which was instead robustly modeled by 1-g fits (this is especially true of low S/N spectra). Therefore, the choice of considering one set of model parameters or the other will depend on the specific problem. We found that diagnostics involving two lines simultaneously (e.g., line-intensity ratios, or linewidths comparisons) were derived much more robustly from 1-g fitting parameters; on the other hand, the description of the gas dynamics considering RVs alone benefitted also from the 2-g model velocities, whenever S/N was sufficient. In this respect, we remark that the smaller thermal widths of the [N II] and [S II] lines permit often a more accurate derivation of components' RVs, despite these lines being weaker than Hα.

In several cases among those shown in Figs. 2 to 4, residuals from 1-g fits showed a blue component. This might be indicative of an approaching ionized layer, blueshifted with respect to the bulk of ionized gas, and reminiscent of the layer in the outer part of the Orion nebula, known as the Veil (see the reviews by O'Dell 2001; O'Dell et al. 2008). More detailed indications on the dynamics of the neutral gas probably associated with this layer in the M 8 nebula are derived from the sodium absorption lines in Sect. 3.2 below.

Some general properties of the ionized gas may be derived from the best-fit parameters. Figure 5a shows a comparison between RVs derived from 1-g fits to Hα and [N II] 6584 Å lines. The same pattern is shown by measurements from pure-sky fibres and from faint stars, confirming that the usage of faint-star spectra introduced no biases in the derived nebular properties. The datapoints scatter is not caused by errors (<1 km s^{-1} as a rule) but is real: in many cases the [N II] RV is less negative than the Hα RV. The velocity of the low-mass stars in the NGC 6530 cluster is $RV = 0.5 \pm 0.2$ km s^{-1} (Prisinzano et al. 2007), which

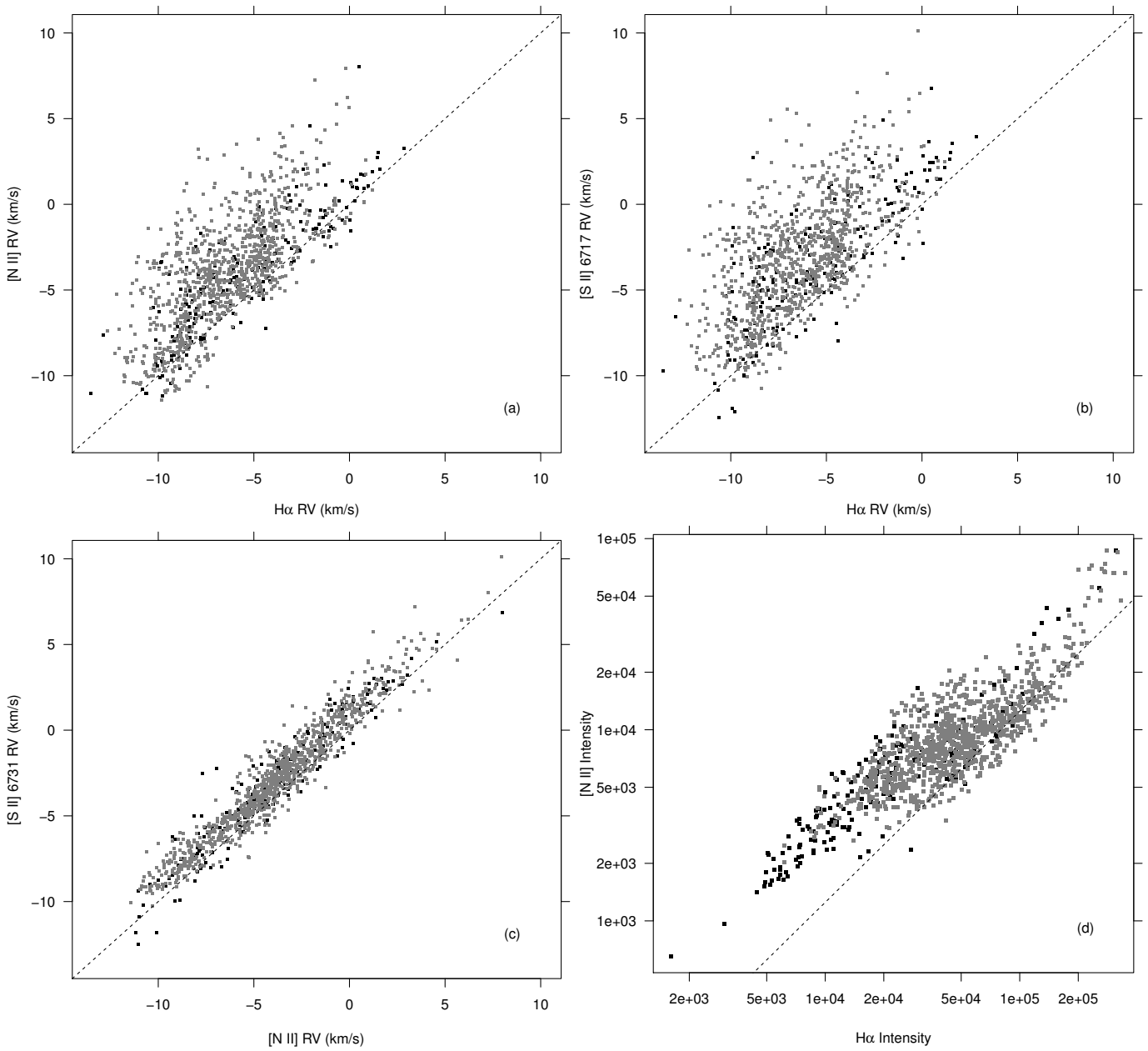

Fig. 5. *a)* Comparison between 1-g best-fit RVs from Hα and [N II] 6584 lines. Black dots indicate pure-sky fibres while gray dots indicate faint stars. The dashed line indicates identity. *b)* Same comparison as in *panel a*, between Hα and [S II] 6731. *c)* Same comparison as in *panel a*, between [N II] 6584 and [S II] 6731. *d)* Comparison between intensities of Hα and [N II] 6584, as resulting from 1-g models. Symbols as in *panel a*. The dashed line represents a ratio of 1/8.

was assumed to coincide with the center-of-mass velocity $RV_{\rm cm}$ of all cluster stars. The figure then shows than the bulk of ionized gas emitting in these lines has negative velocities (approaching us) from the standpoint of the cluster center of mass. This is unlike the case of the Carina nebula, where the double emission line peaks bracket usually the center-of-mass RV, indicating expansion toward both the near and far sides (Damiani et al. 2016). In NGC 6530, the ionized gas seems instead to expand predominantly toward our side (but more details will be studied in Sects. 3.3 and 3.4 below). Figure 5a however shows that along some sightlines the [N II] moves away from us, while hydrogen moves toward us: clearly, the different lines arise from dynamically distinct gas layers, a feature which cannot be understood from narrow-band images, which mix emission from all velocity layers (e.g., Tothill et al. 2008, Fig. 4). The comparison between Hα and [S II] RVs in Fig. 5b shows a pattern very similar to Fig. 5a. This suggests that the [N II] and [S II] lines originate from gas layers which are more closely related mutually than with Hα. This is confirmed by the good correlation shown in Fig. 5c, between the [N II] and [S II] RVs, the small systematic shifts being attributable to the uncertainty in the adopted line wavelengths[1]. This figure also permits to estimate empirically the maximum errors in the best-fit RVs from the scatter of datapoints in the correlation, on the order of $\leq$1 km s^{-1}. We remark that the [S II] and [N II] lines are the weakest being studied, the Hα line being much stronger; therefore, the scatter of datapoints in both Figs. 5a and b is certainly dominated by real effects.

[1] Wavelengths adopted here are 6583.43 Å for [N II], and 6716.44, 6730.815 Å for [S II], the latter two from Kaufman & Martin (1993).

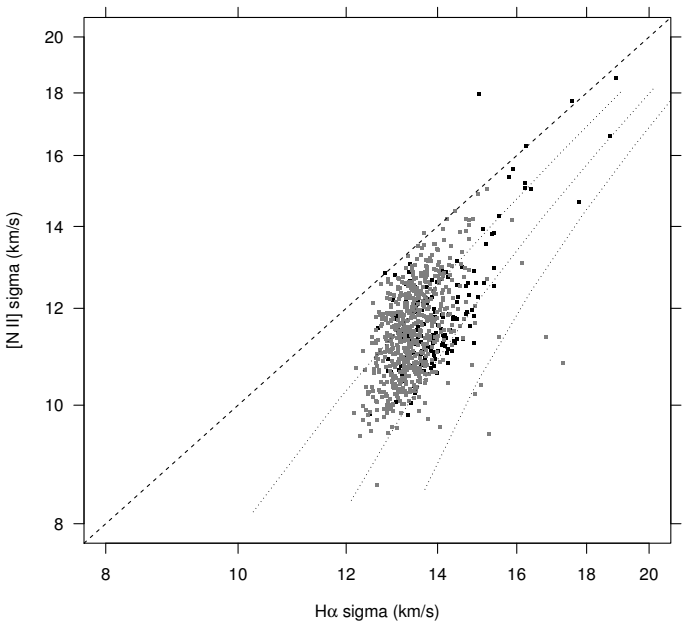

Fig. 6. Comparison between line widths σ of Hα and [N II] 6584, as resulting from 1-g models. Symbols as in Fig. 5. The dotted lines indicate loci of thermally broadened lines for T = 5000, 10 000, and 15 000 K, respectively from left to right. The dashed line represents identity.

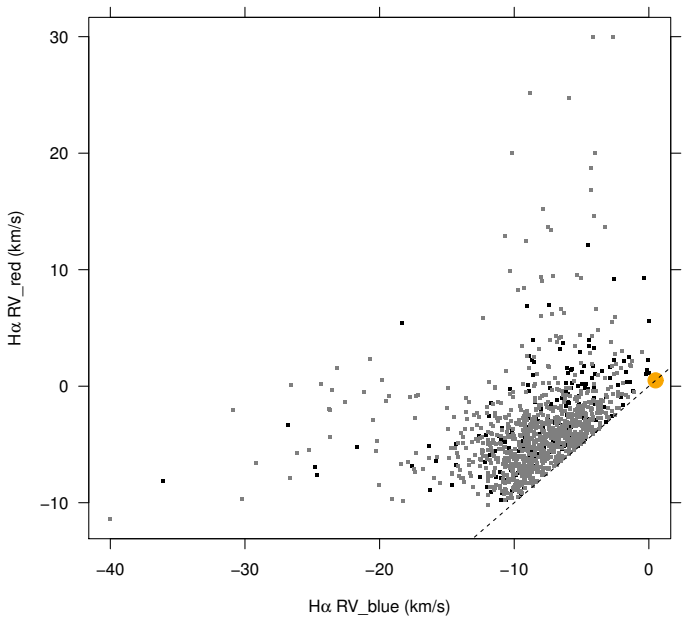

Fig. 7. Comparison between RV of blue and red components as resulting from 2-g model fits of the Hα line. Symbols as in Fig. 5. The orange circle indicates $RV_{\rm cm}$ of late-type cluster stars in NGC 6530, from Prisinzano et al. (2007).

The above results are reminiscent of those found in the Orion nebula, a well studied blister H_{II} region, where ionized gas flows away from the ionization front, and ionized hydrogen is found at more negative speeds with respect to [N II] and [S II], the ionization level gradually increasing as the gas acquires larger and larger speeds in a champagne-flow geometry (e.g., Balick et al. 1974; O'Dell et al. 1993). The analogy with the Orion nebula, although very interesting, cannot however be pushed too far, since there are also important differences between it and M 8: this latter is a much larger region, with more than one ionizing O-type star, and is probably also a more evolved blister, where at least the most massive star 9 Sgr has excavated a larger cavity in the parent cloud compared to that excavated by the Orion most massive member, θ^1 Ori C. We will examine in more detail the relative geometry of 9 Sgr and the M 8 nebula in Sect. 3.3.2.

A comparison between the 1-g model intensities of Hα and [N II] lines is shown in Fig. 5d. The intensity ratio is significantly non-uniform; this, under the typical conditions found in H_{II} regions, suggests significant differences in the ionization parameter across the region (e.g., Viironen et al. 2007), which will be studied in Sect. 3.3. In very general terms, in regions with high Lyman-continuum flux ionization will be highest, and hydrogen lines dominate over [N II] lines; in the same regions, the diagram suggests that the highest densities and largest surfact brightnesses are also found. In Sect. 3.3 we will examine in much better detail how these quantities depend on position across the nebula. Figure 6 shows the best-fit linewidths σ of Hα and [N II], whose comparison provides a measure of temperature (since turbulent and instrumental broadenings are the same for the two lines). To avoid mixing unrelated gaseous layers, we only showed datapoints having maximum absolute RV differences of 3 km s^{-1} between the two lines. In the figure, dotted lines indicate loci for fixed temperatures of 5000, 10 000, and 15 000 K, and a range of combined turbulent+instrumental broadening (between [8–18] km s^{-1}). Most datapoints lie between 5000–10 000 K, however with considerable spread.

We then examined the details of line profiles, as provided by our 2-g best-fit models. In Fig. 7 the RV of the blue component is compared with that of the respective red component in the same spectrum. Also these more detailed RVs show motions predominantly toward us (as seen from center of mass); only a small number of spectra showed blue and red RV components lying on opposite sides of $RV_{\rm cm}$ (i.e., $RV_{\rm red} > 0.5$ km s^{-1} and $RV_{\rm blue} < 0.5$ km s^{-1}), as it would be expected for an expansion originated from center of mass velocity. In the large majority of cases, the two components, both approaching us, have RVs differing by only few km s^{-1}, whose physical origin is not completely clear. One possibility is that the two components are actually an oversimplification of reality, and that they only represent the approximate RV range found in a rapidly decelerating layer emitting Hα. This accounts well for the significant correlation found in Fig. 7 between $RV_{\rm red}$ and $RV_{\rm blue}$ in the Hα line[2]. The median intensity of the blue component is only slightly higher than that of the red component (1.3 to 1.5 times, from pure-sky and faint-star fibres respectively), thus backscattering from dust is unlikely to account for the bulk of the red component.

Still different is the picture derived from the corresponding diagram involving the [N II] line (Fig. 8). Motion receding from us is much more frequently found, and the correlation between $RV_{\rm red}$ and $RV_{\rm blue}$ is much less tight, if existing at all. The blue and red components of [N II] are therefore in many cases indicative of dynamically distinct gas layers, whose spatial characteristics will be examined in detail in Sect. 3.3. It is interesting to compare the RVs for the Hα and [N II] lines, as given by the 2-g fits, analogously to the 1-g RV comparison of Fig. 5a. This was done in Fig. 9: here we see that, unlike the 1-g fit RVs, there is in most cases a fairly good match between RVs of the two lines, apart from a minority of strong outliers. In order to reconcile this

[2] Alternatively, this might be an instrumental effect arising from the non-Gaussianity of the line-spread-function, a systematic effect that becomes observable at the highest signal levels, see Damiani et al. (2016, Appendix).

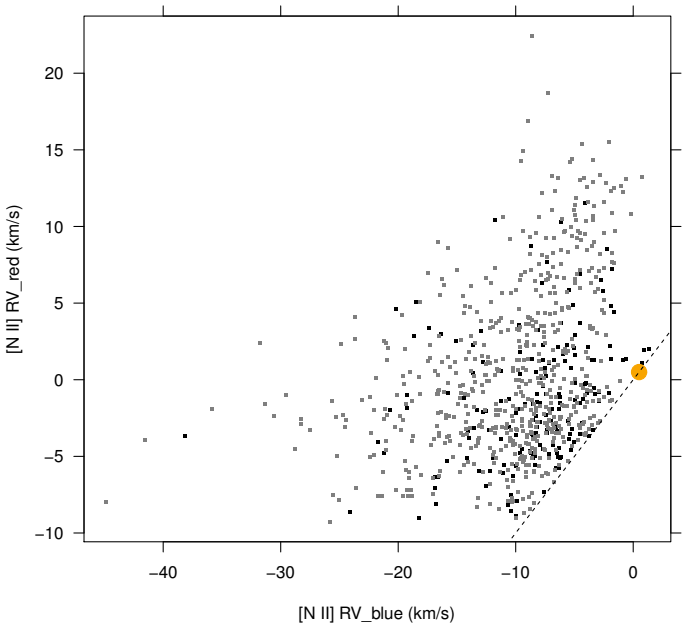

Fig. 8. Same as Fig. 7, for the [N II] line.

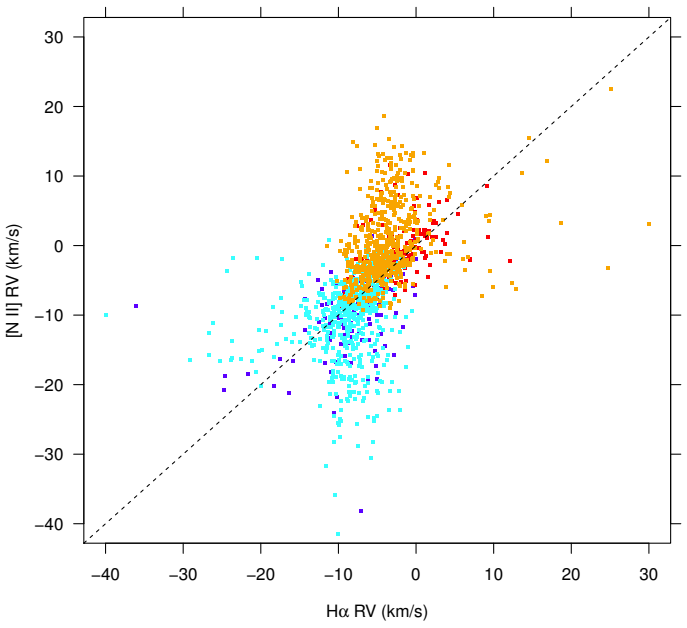

Fig. 9. Comparison between RVs of Hα and [N II] 2-g fits. The results of each individual spectrum are plotted twice, once for the red Hα and [N II] components, and again for the blue components of the same lines. Blue and red dots refer to blue and red components from sky fibres, while cyan and orange dots refer to the same components from faint stars.

agreement with the disagreement of 1-g RVs shown by Fig. 5a, one may expect that the relative intensities of the blue and red components are different between Hα and [N II], with the red component being dominant in [N II] over Hα, and viceversa for the blue component. This expectation is confirmed by the diagram of Fig. 10, where the intensities of the different lines were compared (for each blue and red component separately). Only components with an absolute RV difference less than 3 km s^{-1} were plotted. It is clear that red components tend to have a larger [N II]/Hα intensity ratio than blue components, and therefore lower ionization, as mentioned above. Recalling the above result that the two components are diagnosing different layers from gas moving in the same direction, we infer that the gas moving faster (larger negative velocities: blue component) is more ionized than the slower red component.

3.2. [O III] and sodium D lines from UVES data

A representative selection of line profiles of the [O III] 5007 Å line[3] from UVES spectra of several stars is shown in Figs. 11 and 12. Although all spectra are from stars and not sky fibres, the nebular line is clearly evident; no stellar spectrum subtraction was performed (apart from a constant continuum level) for any of the spectra shown. This line is frequently the second strongest nebular line in our spectra, after Hα. In the [O III] line doubly-peaked profiles are much more frequently found (as already reported by Elliot & Meaburn 1975) than in lower-ionization lines like those of [N II]. Even if no double peaks are found, line distortions are evidently present in most cases, and required 2-g fits. In only one case (labeled star 520-5, upper left panel in Fig. 12) two Gaussians provided a bad fit (as shown), and three components are suggested by the line profile: this is the O7 star Herschel 36 in the Hourglass nebula, having also the strongest [O III] line among our sample. Shown with green lines in Figs. 11 and 12 are our 2-g model fits, which reproduce the [O III] profiles very well, except for Herschel 36.

[3] The exact wavelength used here is 5006.843 Å, from NIST (http://physics.nist.gov/asd, Kramida et al. 2015).

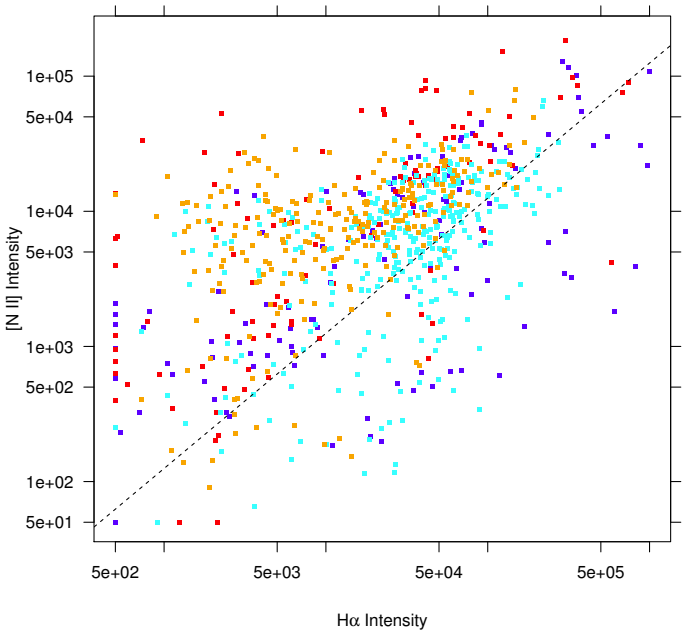

Fig. 10. Comparison between intensities of Hα and [N II] (log scales), from 2-g fits. Symbols as in Fig. 9.

The UVES spectra of stars in NGC 6530 also enabled us to study the neutral gas along the line of sight to these stars, using the sodium D doublet. The selection of UVES targets in the *Gaia*-ESO Survey was such as to maximize the probability of their cluster membership (Bragaglia et al., in prep.); therefore, most (not all) UVES spectra are likely to sample the entire column of neutral sodium between us and NGC 6530. A wide selection of sodium absorption line profiles for these stars is presented

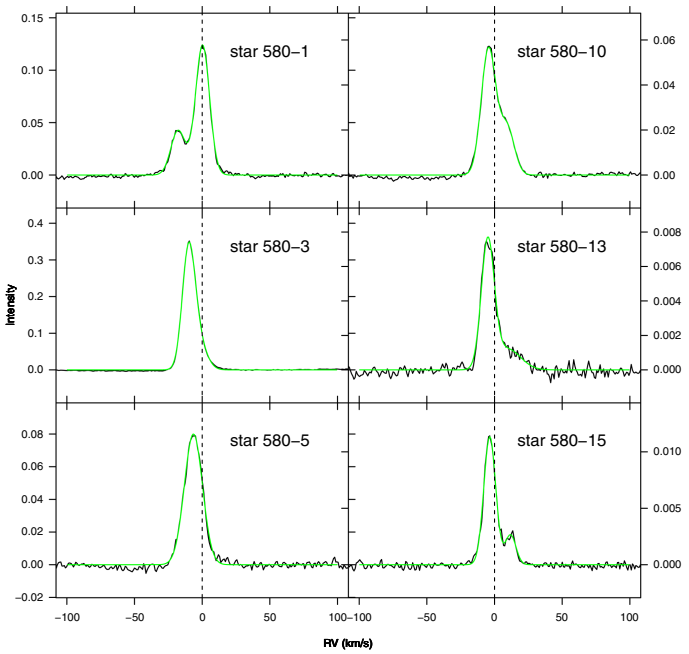

Fig. 11. Line profiles (black) and 2-g best-fit models (green) for the [O III] 5007 line, from UVES stellar spectra.

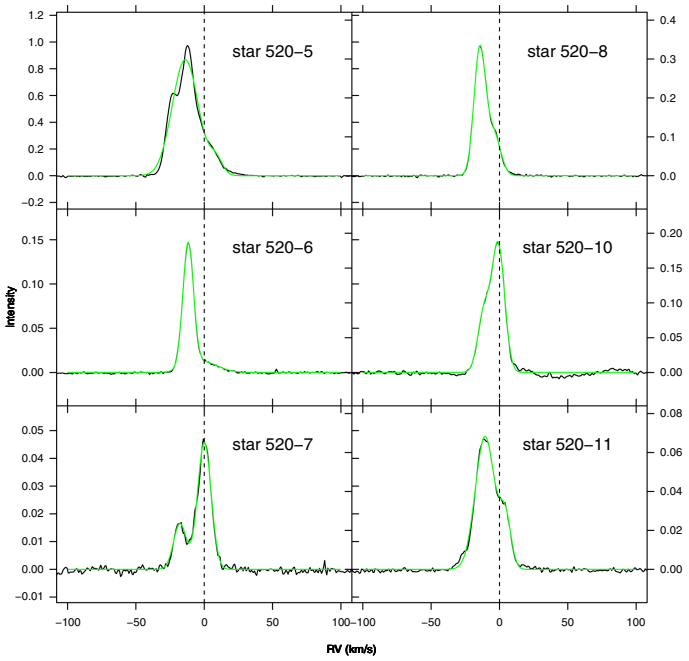

Fig. 12. Additional [O III] line examples, as in Fig. 11. Star 520-5 is the O star Her 36, the only case in which the two-Gaussian profile fails to match well the observed profile.

in Fig. 13. For not-too-hot stars, the stellar sodium lines were also evident in the spectra: these were divided out, using suitable template spectra chosen among the UVES-POP library (Bagnulo et al. 2003), such that Fig. 13 shows only non-stellar absorption components. Both doublet lines are shown, the D1 line in black, and the stronger D2 line in red. The occasional features at ∼10 and 30 km s^{-1} in the D1 line (only) are telluric. The intensity ratios of the two lines are closely related, being originated from the same (ground) level, and having oscillator strengths of $f_{D2} = 0.6405$ (D2) and $f_{D1} = 0.3199$ (D1). The low ionization energy of sodium (5.139 eV) implies that these lines must originate from layers more distant from the OB stars (nearer to us) than the ionic lines studied in Sect. 3.1. In basically all cases, more than one absorbing layer, each with a distinct RV, is needed to model the sodium absorption profiles. The most complex line profiles are modeled with five Gaussians.

The fitting function was chosen as follows: we rewrite Eq. (1) from Hobbs (1974) using λ instead of ν as (for a single component)

$$N\frac{\pi e^2}{m_e c}\frac{\lambda^2}{c}f = N\int \alpha_\lambda \,\mathrm{d}\Delta\lambda = \int(-\ln r_\lambda)\,\mathrm{d}\lambda, \tag{1}$$

and the term containing the residual intensity r_λ, for a combination of absorbing layers i, as

$$\int(-\ln r_\lambda)\,\mathrm{d}\lambda = \sum_i N_i \int \frac{1}{\sqrt{2\pi}\sigma_i}\exp\left(-\frac{1}{2}\frac{(\lambda-\lambda_i)^2}{\sigma_i^2}\right)\mathrm{d}\lambda, \tag{2}$$

where $\lambda_i = \lambda_0 + v_i/c$ is the central wavelength of absorbing component i, at velocity v_i, and λ_0 is the line rest wavelength. σ_i is the component intrinsic width in wavelength units. The explicit form for r_λ is therefore:

$$r_\lambda = \exp\left(-\sum_i \frac{N_i}{\sqrt{2\pi}\sigma_i}\exp\left(-\frac{1}{2}\frac{(\lambda-\lambda_i)^2}{\sigma_i^2}\right)\right). \tag{3}$$

Since the lines from cold neutral sodium may be very narrow, and saturated absorption profiles may become highly non-Gaussian, the instrumental resolution of UVES was separately introduced as a fixed Gaussian broadening through convolution, and the final functional form used to fit the observed, normalized line profiles is:

$$r_\lambda^{\mathrm{obs}} = r_\lambda \otimes \int \frac{1}{\sqrt{2\pi}\sigma_{\mathrm{UVES}}}\exp\left(-\frac{1}{2}\frac{\Delta\lambda^2}{\sigma_{\mathrm{UVES}}^2}\right)\mathrm{d}\Delta\lambda, \tag{4}$$

where $\otimes$ is the convolution operator and σ_{UVES} (∼2.7 km s^{-1}) is the UVES instrumental linewidth. The chosen function for r_λ corresponds to absorption from cold gas, whose emissivity is approximated as zero. Using this function, non-linear fits were attempted to the D2 line profiles (the strongest of the doublet) with two to five components; the optimal number of fitting components was determined by inspecting the results visually. The chosen best-fit models of D2 lines are superimposed to the observed profiles in Fig. 13 as orange curves: these match so well the observed profiles as to result often indistinguishable from them. Velocities of the individual best-fit components are indicated in the figure. They range from ∼−50 km s^{-1} to ∼+10 km s^{-1}; however, positive-velocity components were found only in two cases, the most evident example being that of star 520–14 in the figure. As it should be clear from Eq. (1), the profiles of the D1 line can be obtained from those of the D2 line (Eqs. (3) and (4)) by multiplying the intensity of each component N_i by the constant factor f_{D1}/f_{D2}. Model profiles of the D1 line obtained in this way are also shown in Fig. 13 as blue lines. In most cases, they match well the observed D1 profiles (black), providing a test of the goodness of the adopted best-fit models. Best-fit parameter values are reported in Table A.2. Intensity values $N_i > 1000$ correspond to saturated components and are highly uncertain.

However, a number of cases were found where the observed D1 profile and its model do not match (see e.g., stars 520-13, 520-14, 520-28, 520-36, 520-39), to a significant degree for the given S/N. The discrepancy occurs always near velocities of ∼−30 to −20 km s^{-1}. It is always in the same sense, with the

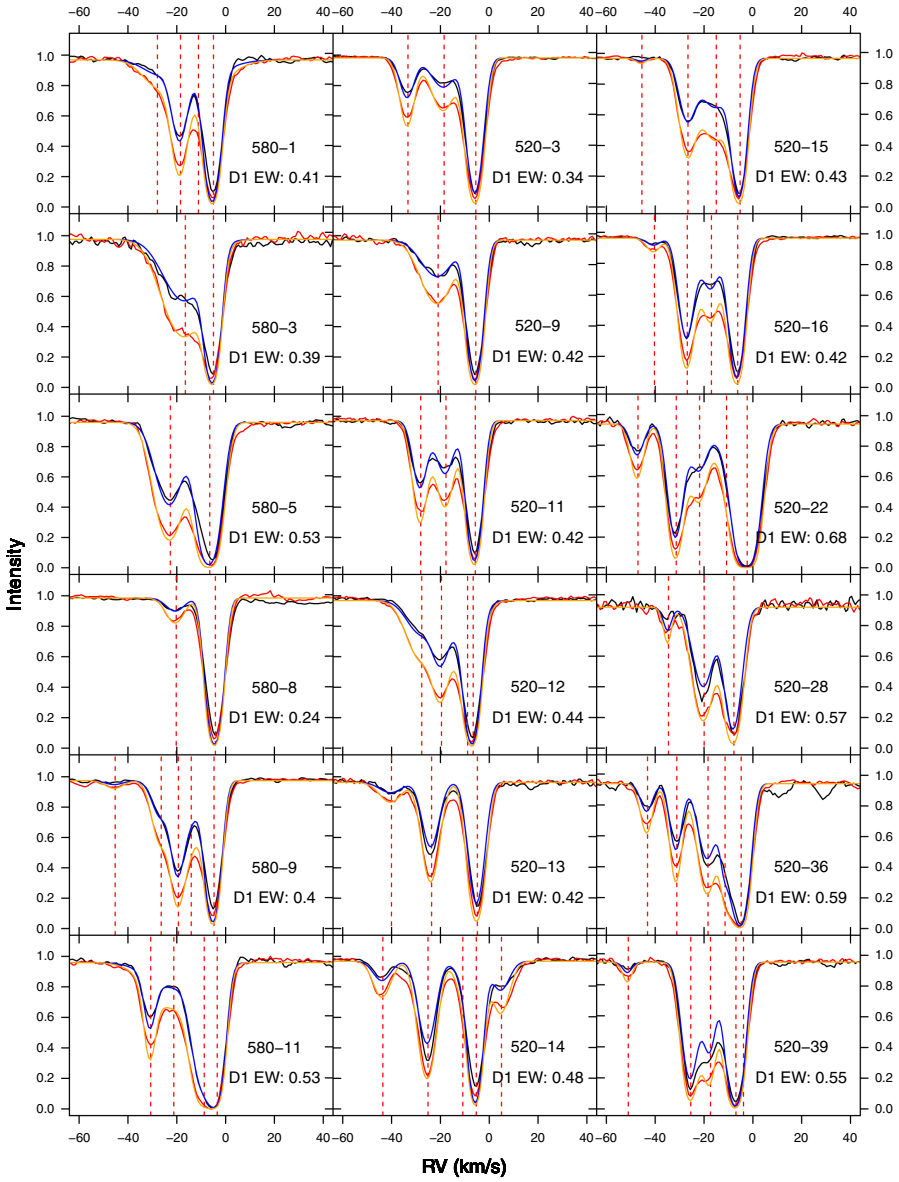

Fig. 13. Profiles of interstellar sodium D1 (black) and D2 (red) lines from UVES spectra (both setups 580 and 520, as labeled). The stellar line contributions, when present, were removed by division with suitable template spectra. The orange curves are multiple-Gaussian best-fit models to the D2 profiles; the blue curves are D1 profile predictions based on the D2 models, and assuming pure absorption (see text). Vertical red dashed lines indicate the best-fit RVs of model components. Total equivalent widths for the D1 lines are also indicated (in Angstroms).

observed D1 profile being deeper and closer to the respective D2 profile than the model would predict: this is suggestive of that particular component saturating toward a finite, non-zero intensity, contrary to the assumption above of zero emissivity. If this latter condition is not met, the profile modeling becomes extremely more complex, the contributions from different layers not being writable as a linear sum in $\ln r_\lambda$; also the order of layers along the line of sight becomes important (the emission of one layer can be absorbed only by the layers closer to us), which is not the case when pure absorption is modeled. We have therefore not modeled those few cases in quantitative detail. Qualitatively, it is suggested that the layers at velocities ~ -30 to -20 km s^{-1} are sometimes hotter than those at lower and higher velocities, their source function being much higher than zero compared to the photospheres of the UVES targets. Temperatures of several thousands K are therefore likely for those particular sodium layers. We consider it likely that these layers are spatially adjacent to those where recombination has recently taken place, as also supported by their similar velocities. The higher temperatures in the sodium layers at ~ -30 to -20 km s^{-1} are also supported by their increased line widths σ, as shown by Fig. 14. We remark that this figure shows intrinsic line widths σ_i, not the observed values, degraded by the instrumental resolution (as in Eq. (4)). For this reason, their lower bound was set to zero in the fitting; however, values of σ_i lower than ~ 3 km s^{-1} should be regarded as upper limits.

The wide variety of absorption profiles found within small angular scales on the sky suggests strongly that the associated neutral gas lies in the immediate vicinity of the Lagoon nebula, and not all along the line of sight. Also the observed large radial velocities of sodium absorption are not expected for the general ISM gas in nearly circular orbits and observed almost in the direction of Galactic center, and further support this argument. The same cannot be said for the strong, saturated component near ~ -5 km s^{-1}, which although not strictly identical in all profiles is so widespread (and consistently narrow) that we cannot rule out a line-of-sight origin. A puzzling feature from the sodium spectra is the clear existence of components at much larger negative velocities than found from the ionic lines in Sect. 3.1: at face value, this would imply that the expanding gas, after recombining at a typical approaching velocity of -5 to -10 km s^{-1} (Fig. 5a), keeps accelerating toward us to produce the neutral layers around -30 to -40 km s^{-1}. Also the origin of the discrete velocity components (as opposed to a continuous velocity

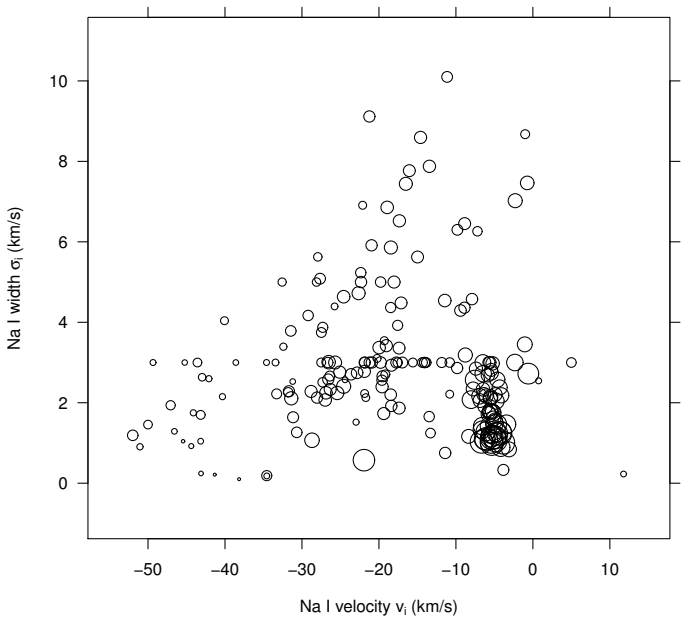

Fig. 14. Sodium absorption linewidths σ_i vs. radial velocities v_i, for all fit components. Circle size is proportional to component intensity.

distribution) in the sodium profiles is unclear, that is whether it is related to a episodic energy input or to different pre-existing layers of neutral gas, swept by the expanding envelope. In the former case, a single star would be driving the phenomenon, or otherwise the uncorrelated input from many stars would produce a smoother velocity distribution. In the second, a continuously (non-episodically) expanding shell would encounter discrete gas layers, and decelerate as more and more mass is being pushed; this seems contradictory with the above suggestion that neutral gas is accelerated outwards, in the sodium-line formation region.

We have also computed equivalent widths for the D1 line (labeled D1 EW in Fig. 13), which fall in the range 0.4–0.6 Å for the bulk of stars. Using the relation given by Munari & Zwitter (1997), this range would imply a $E(B-V)$ range of 0.2–0.5, in good agreement with that found by Sung et al. (2000) for the NGC 6530 massive stars.

3.3. Spatial maps

Most of the properties characterizing the nebular emission, as derived from the line modelization discussed in Sect. 3.1, show distinct spatial patterns, which we examine in detail here. Figure 15a shows a map of the [N II]/Hα intensity ratio (proportional to symbol size), superimposed on a VPHAS+ image of the nebula as in Fig. 1. As mentioned in Sect. 3.1, a smaller intensity ratio corresponds to higher ionization parameter. While one would expect the latter to increase in the vicinity of the hottest stars, this is not always found in our data. Not considering the two O stars near the east (HD 165246) and west (HD 164536) edges of the nebula, where our spatial coverage is sparse, we observe a clear ionization increase around HD 165052 (in south-east region), while the bright nebula surrounding the Hourglass shows no clear ionization pattern around its three O stars (north to south: HD 164816, 9 Sgr, and Herschel 36). The darker nebula parts (called the Great Rift in Lada et al. 1976) around this brightest region shows distinctly higher ionization than near the Hourglass. The relatively low ionization near 9 Sgr supports further the suggestion by Lada et al. (1976) that this star should lie several pc in front of the nebular material, not in its immediate vicinity. The irregular ionization near Herschel 36, instead, can be attributed to the patchy distribution of dense gas and dust all around this star, as suggested by the HST image of the Hourglass (Tothill et al. 2008). Near the central NGC 6530 cluster, to the S-E of the Great Rift, ionization is often higher than in the Hourglass region; however, there seems to be a gradient across the cluster, not a peak near its center, so that the source of ionization is probably not internal to the cluster, with the best candidate remaining the O4 star 9 Sgr, despite being a few parsecs away. The issue will be examined in more detail in Sect. 3.3.2 below. The bright blue supergiant HD 164865 (B9Iab) probably contributes to ionization locally, but not predominantly since there is no associated ionization peak near it.

We next considered the nebular electron density, as measured from the ratio of [S II] 6717, 6731 Å lines (Fig. 15b). The spatial pattern is here very different than the ionization pattern: a strong and distinct increase in density ($\sim 3000 \times \sqrt{10^4/T}$ cm^{-3}, in agreement with Bohuski 1973) is found throughout the vicinity of the Hourglass, with the peak coinciding with the Hourglass proper. The agreement between line ratios from pure-sky fibres and faint-star spectra is very good, which is especially crucial here because of the near coincidence between the [S II] 6717 line and a Ca I photospheric line. A very localized enhancement in density is also found in the immediate vicinity of the bright rim near M 8E-IR (S-E of NGC 6530). Near the stellar cluster core, instead, the density is not particularly high ($\sim 800 \times \sqrt{10^4/T}$ cm^{-3}), not higher than in the neighboring Great Rift, despite the large difference in nebular brightness. The density decreases very smoothly toward the nebula edges, to $\sim 50 \times \sqrt{10^4/T}$ cm^{-3}. The density was derived from the doublet ratio using analytic expressions in Weedman (1968) and Saraph & Seaton (1970).

The radial velocity map for Hα, shown in Fig. 16 provides a vast amount of information. Velocities are here those derived from 1-g fits. Since $RV_{\rm cm} \sim 0$, absolute velocities are nearly the same as $|RV - RV_{\rm cm}|$, that is referred to the NGC 6530 center of mass. There is no central symmetry in the velocity field. The cluster core nearly coincides with a (negative) velocity maximum: absolute velocities decrease toward both S-E and N-W from this position. The location of these low-absolute-velocity datapoints defines a reference direction, indicated with a red arrow in the figure; this is almost coincident with the normal to the galactic plane. The galactic plane itself is just off the figure region to the right. The Hourglass region is also characterized by large negative velocities, but no velocity minimum is detected west of it, probably also because of the incomplete spatial coverage. In the outermost nebula regions to the east the velocity smoothly decreases toward $RV_{\rm cm}$. However, this does not happen in the western edge, where velocities remain at large negative values, a surprising fact which will be discussed in more depth in Sect. 3.4.3.

The velocity map obtained from the 1-g [N II] line fits is instead shown in Fig. 17: although it presents many similarities to the analogous map for Hα of Fig. 16, there are also important differences: in the Hourglass region the negative velocity maximum is much less pronounced; on the contrary, in the Great Rift even positive velocities are found. That is, the Hα and the [N II] lines in this region indicate gas moving in opposite directions with respect to the cluster center-of-mass velocity $RV_{\rm cm} = 0.5$ km s^{-1}. In the N-W part, the puzzling large negative velocities are again found.

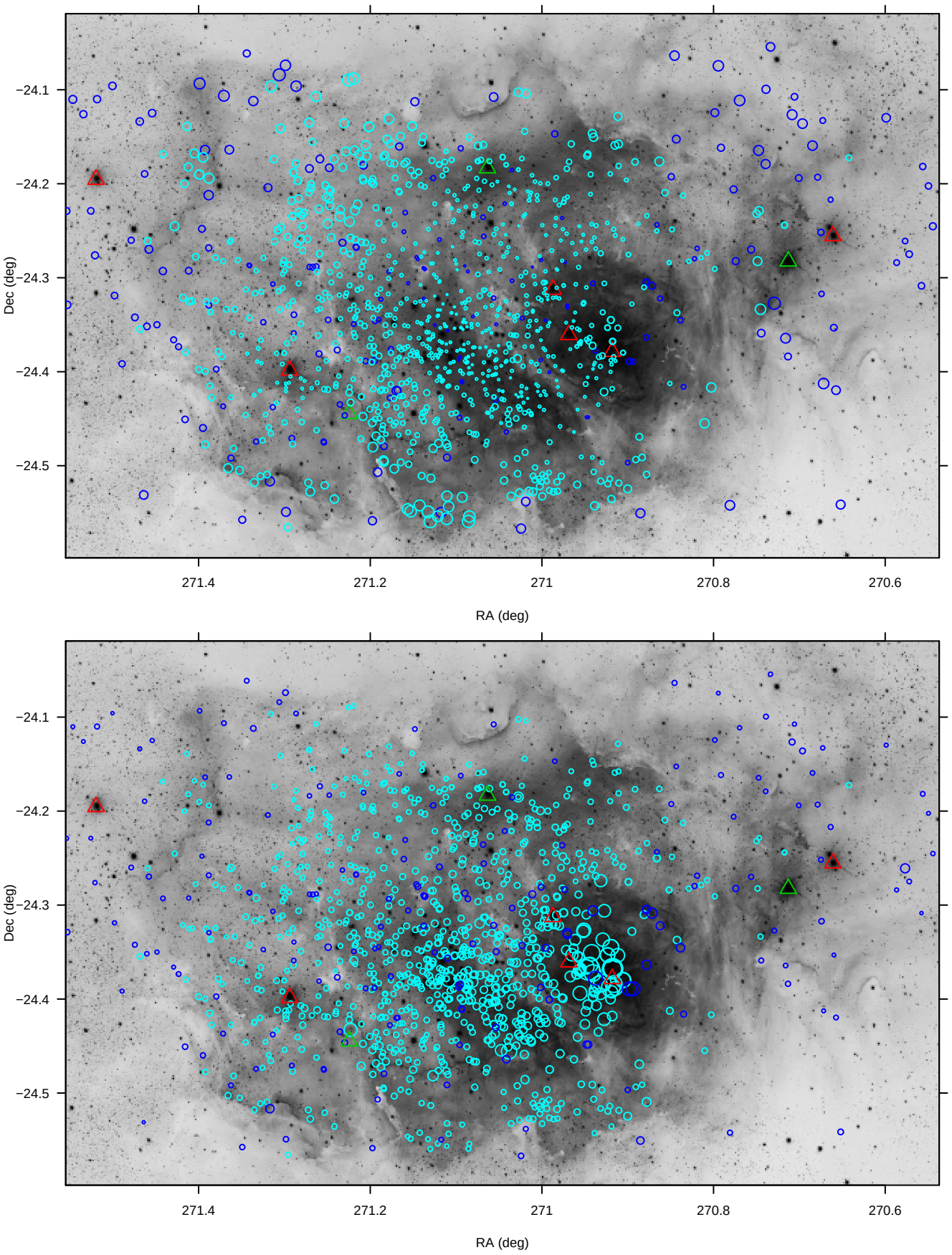

Fig. 15. *a)* (*Upper panel*) map of intensity ratio between [N II] and Hα (proportional to circle size) from 1-g model fits, superimposed to the same VPHAS+ image as in Fig. 1. Blue (cyan) circles refer to pure-sky (faint star) fibres. Triangles have the same meaning as in Fig. 1. *b)* (*Lower panel*) map of [S II] 6731/6717 intensity ratio (proportional to circle size, and increasing with density). Symbols as in *panel a*.

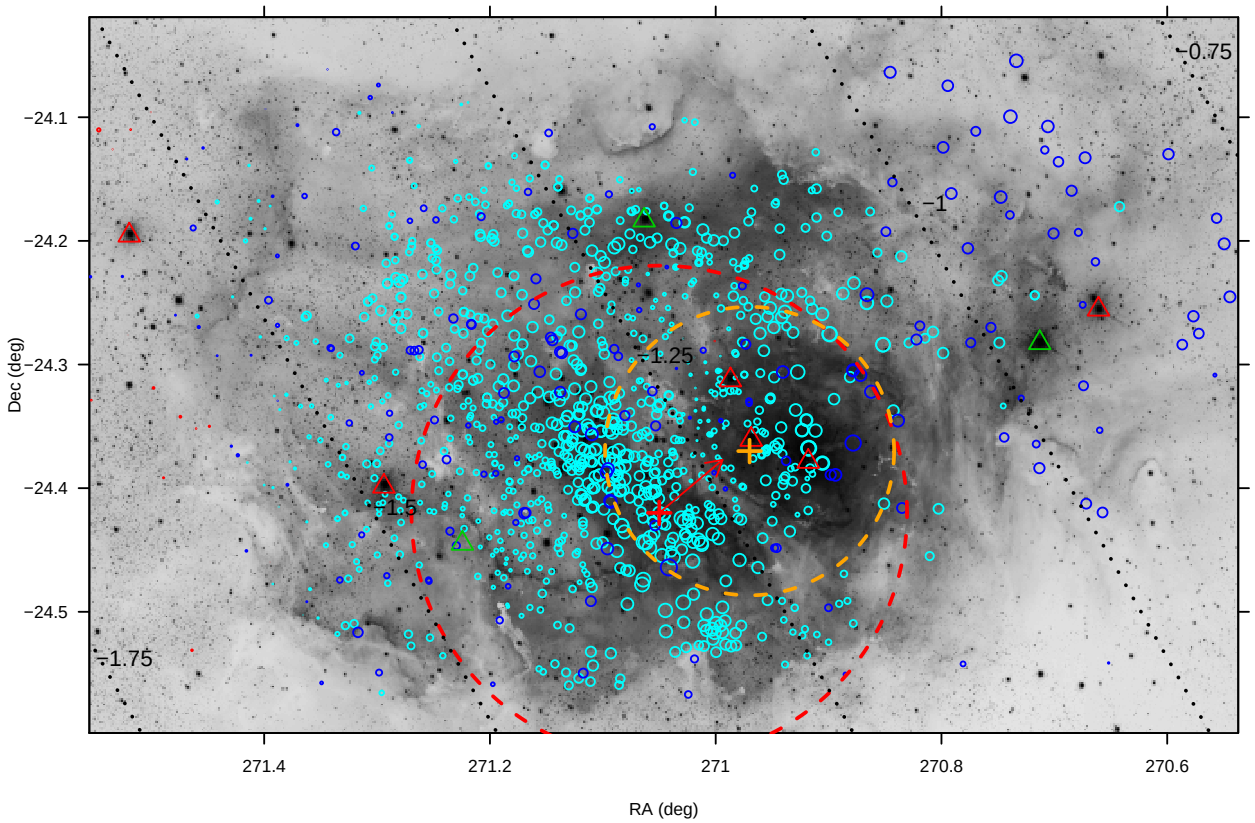

Fig. 16. Map of Hα RV (absolute value proportional to circle size) from 1-g model fits. Blue (cyan) circles: negative-velocity values from sky (faint-star) fibres; red circles: positive-velocity values (only a dozen datapoints, all near zero velocity and lying close to the eastern edge). Triangles have the same meaning as in Fig. 1. Oblique dotted lines indicate Galactic latitudes $b = -1.75$ (left) to $b = -0.75$ (right), in steps of $\Delta b = 0.25$. Plus signs indicate reference positions for the NGC 6530 core (red) and Hourglass region (orange). Centered on these positions, two dashed circles are shown, of radii 12′ (red) and 7′ (orange), respectively. The red arrow indicates the direction of steepest RV gradient around the cluster core, nearly orthogonal to the galactic plane.

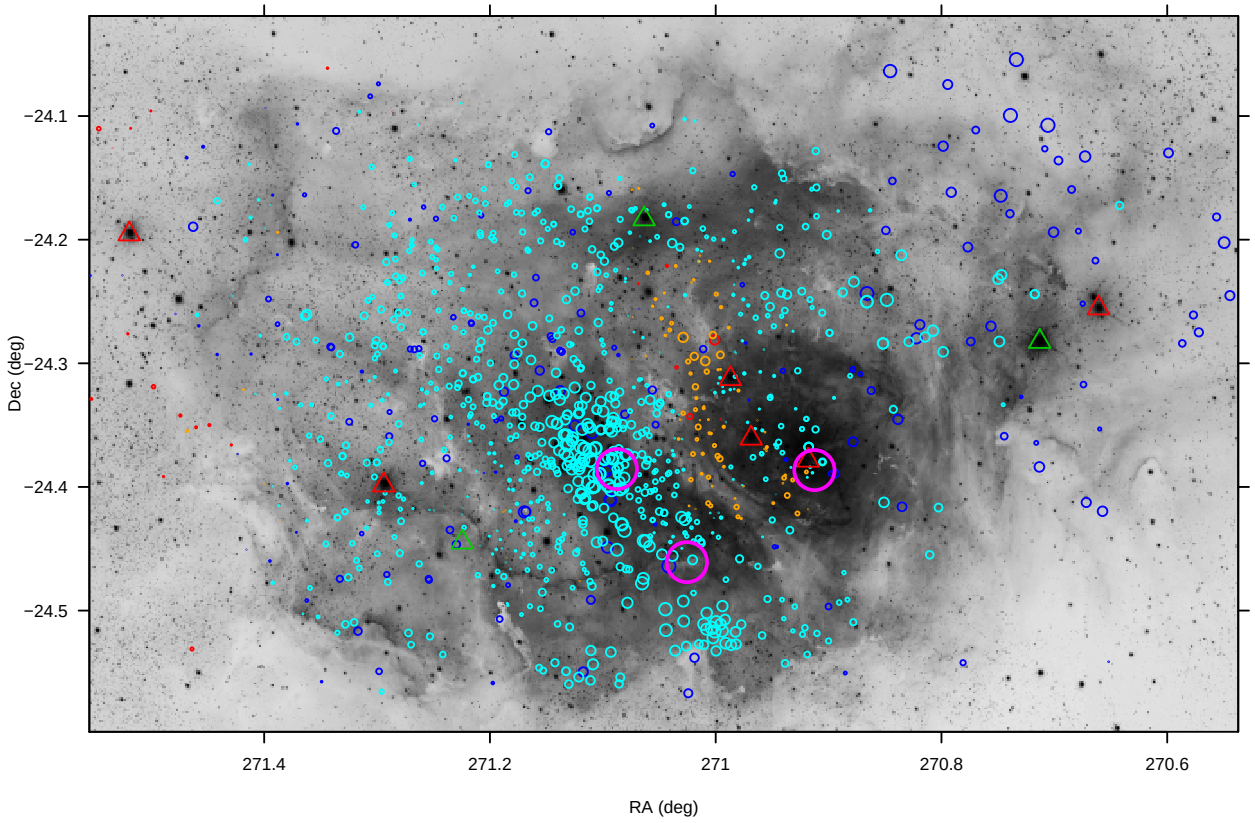

Fig. 17. Map of [N II] RV from 1-g model fits, analogous to Fig. 16, with same meaning of symbols, plus orange circles representing positive-velocity datapoints from faint-star fibres. The three large magenta circles indicate the positions of the CO bright spots found by Lada et al. (1976).

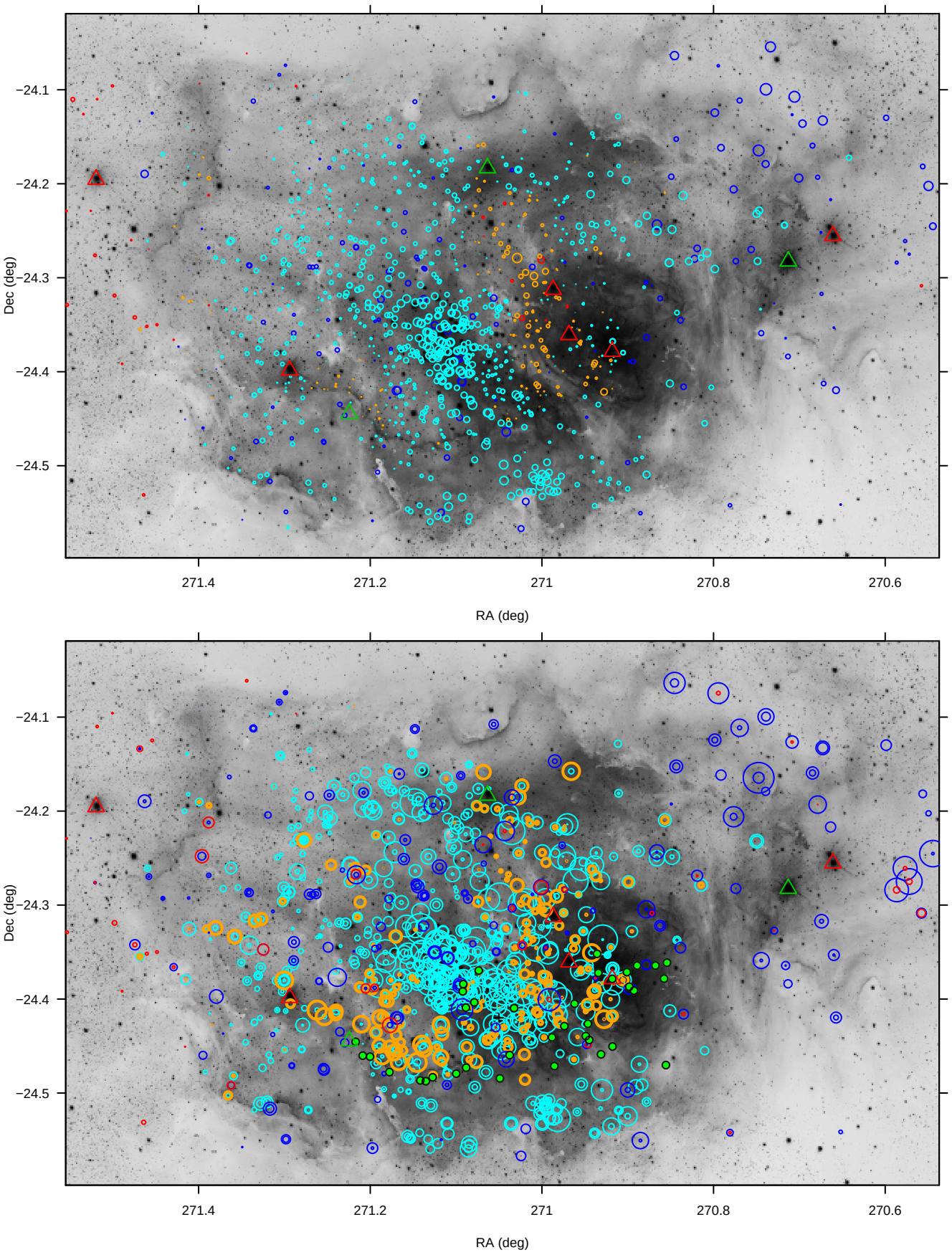

Fig. 18. *a)* (*Upper panel*) map of [S II] RV from 1-g model fits, analogous to Figs. 16 and 17, with same meaning of symbols. *b)* (*Lower panel*) map of [N II] RV (absolute value proportional to circle size) from 2-g model fits. Symbols as in *panel a*, with the addition of green filled dots indicating the submillimeter clumps found by Tothill et al. (2002). Concentric circles of same color indicate that both RV components have the same sign.

The [S II] velocity map of Fig. 18a confirms these trends even more, with slightly positive velocities being found also to S-E of NGC 6530 cluster core, almost parallel to the Great Rift. The positive-velocity datapoints in this region follow closely the inner border of the bright-rimmed dark cloud hosting the massive protostar M 8E-IR, while velocities just outside the bright rim (i.e., projected against the most obscured part) become suddenly negative. Again, the sharpest velocity gradients occur along a line joining M 8E-IR with the Hourglass region (arrow in Fig. 16), so that a more detailed understanding can be achieved from considering position-velocity diagrams along this direction. Before doing that, however, we consider the spatial maps obtained from results of the 2-g fits.

A 2-g velocity map for [N II] is shown in Fig. 18b. We preferred to study this line with respect to the brighter Hα because the narrower line widths permit a better determination of individual component velocities. We have omitted the weakest components, which contribute more to the noise than to show a clear pattern. The most important features shown are the crowdings of positive-velocity datapoints near M 8E-IR and along a vertical strip passing through 9 Sgr and Hourglass. Also indicated are the positions of the sub-mm knots found by Tothill et al. (2002; they did not explore the northern half of the nebula): the orange datapoints fill almost exactly the arc-shaped region delimited to the south by those knots, and ending with M 8E-IR to the east. Also the orange datapoints in the Hourglass region tend to fill the interior of a region delimited by the sub-mm knots to the south. Almost everywhere else, no receding component (with respect to $RV_{\rm cm}$) is observed in the ionized gas, even considering the 2-g line profile models.

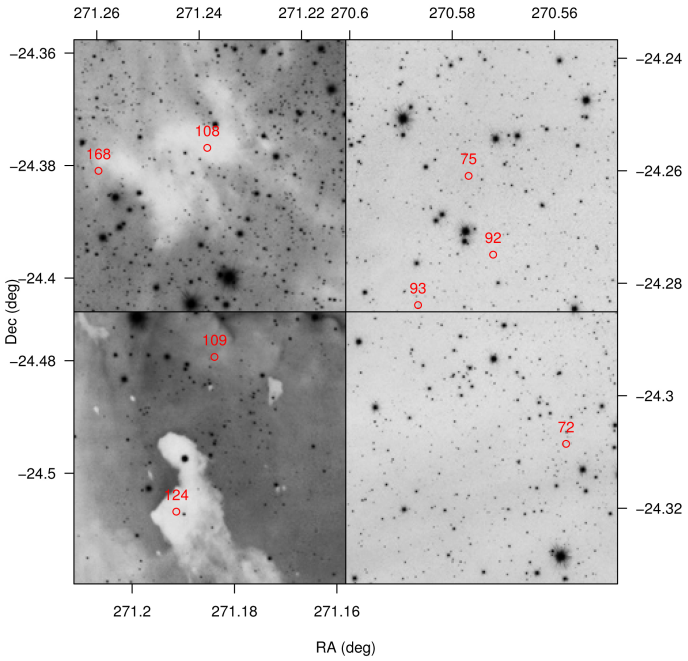

Fig. 19. Examples of dark globules projected against bright background (*left*), and the extreme west of the nebula. Sky fibre positions (only) are indicated, for some of which spectra are shown in Fig. 4 and discussed in the text.

3.3.1. Peculiar locations

The image of the nebula shows several dark globules or "elephant trunks" projected against the bright nebular background. For some of these dark nebulae we have fibre spectra, enabling us to discriminate the properties of the foreground gas against that of the brighter background. Two such examples are shown in Fig. 19, left panels. The one in the lower left panel (called the Dragon by Brand & Zealey 1978; and Tothill et al. 2008) is one of the most evident, and its spectrum was shown in Fig. 4, labeled as Nr. 124. This latter reveals that the nebular emission, although attenuated by a factor ∼10 with respect to adjacent unobscured positions, is still substantial, and images show it as dark only because of the sharp contrast with the surrounding bright emission; nevertheless, this spectrum shows a peculiar component, as a significant emission residual at velocity ∼−50 km s^{-1}. This is not seen, at least not as clearly as here, in any other spectrum, including those of other obscured patches like that in the upper left panel of Fig. 19. Therefore, at least in the direction of the Dragon, we see that ionized gas with velocity ∼−50 km s^{-1} exists above a distance from the nebula enclosing ∼90% of the bulk emission, from simple aperture photometry with respect to nearby unobscured positions. The existence of faster gas component at large distances agrees with the results from the sodium lines presented in Sect. 3.2, and with those of Meaburn (1971) on [O III] lines.

The right panels of Fig. 19 show instead the locations, in the extreme west of the entire nebula, where the most asymmetric or even splitted line profiles are found in our dataset (spectra labeled as Nr. 72, 92, 93 both here and in Fig. 4); here again the nebular emission is so weak as to appear nonexistent in the narrow-band image, but is enough to be detected and studied in our spectra. Figures 4 and 19 together show that the nebular line profiles vary smoothly with spatial position, which confirms that their peculiarities do not arise from some random effect, or isolated cloudlet. We will discuss therefore the implied large-scale motion of this part of the nebula in Sect. 3.4.3.

3.3.2. The position of 9 Sgr

Another peculiar location is that of the most massive star, 9 Sgr, which as mentioned is suspected to lie at some distance (5–10 pc according to Lada et al. 1976) in front of the cloud. Assuming like these authors that it is the dominant ionizing source for the entire nebula (i.e., except in the vicinity of Herschel 36 or HD 165052), its line-of-sight distance from the nebula may actually be estimated from the decay of measured ionization with sky-projected distance. We are able to estimate the ionization parameter q from the Hα/[N II] ratio, using for example the curves shown by Viironen et al. (2007), and the electron density $N_{\rm e}$ from the [S II] doublet ratio. The product $qN_{\rm e}$ is proportional to ionizing flux F; this will follow a spatial decay like $F = I_0/(r^2 + d_{\rm rad}^2)$, where r is the sky projected distance from 9 Sgr, and $d_{\rm rad}$ is the line-of-sight distance of 9 Sgr from the nebula, assumed flat. Figure 20 shows the result of this experiment: a well defined peak is indeed found, with additional, local enhancements in ionizing flux near +3 and −20 arcmin due to Herschel 36 and HD 165052, respectively; a minor enhancement near −9 arcmin corresponds instead to the B stars in the NGC 6530 core. The proposed functional form for F is shown by the lines, with the green one corresponding to 3 arcmin, or $d_{\rm rad}$ = 1.09 pc at the nebula distance. If the adopted curve maximum is lowered, to account for the fact that the actual maximum in the datapoints is due to Herschel 36, a 4-arcmin curve is also satisfactory, corresponding to $d_{\rm rad}$ = 1.46 pc. These normal distances are much smaller than the estimates by Lada et al. (1976); one possible explanation is the assumed planar geometry for the illuminated nebula: a slightly convex geometry would increase center-to-edge differences, and require larger $d_{\rm rad}$ to produce the

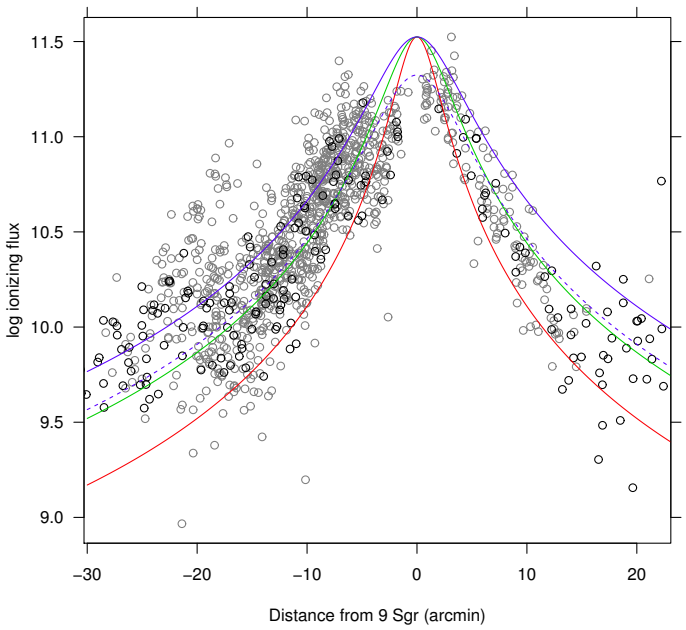

Fig. 20. Ionizing flux vs. radial distance from 9 Sgr, shown separately for the eastward and westward directions (negative and positive distances, respectively). Black (gray) dots refer to pure-sky (faint star) fibres. The blue, green, and red solid lines refer to normal distances of 1.46, 1.09, and 0.73 pc, respectively. The blue dashed line refers to a distance of 1.46 pc, adopting a different maximum flux.

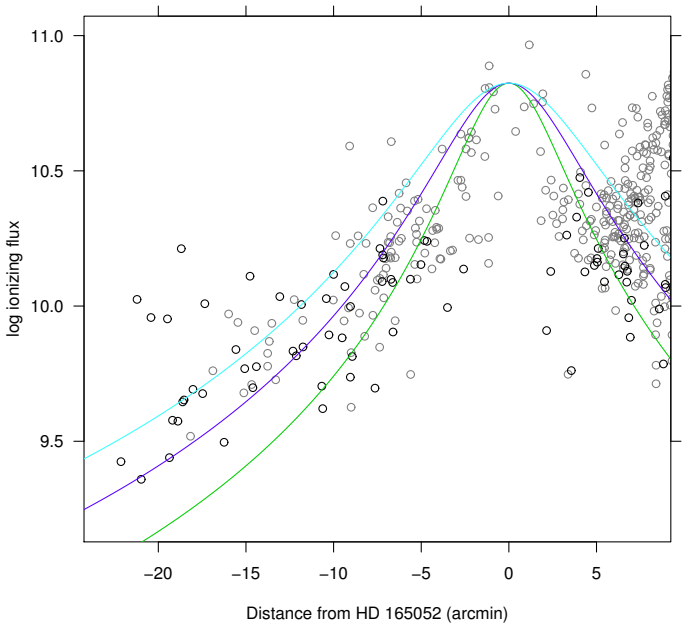

Fig. 21. Ionizing flux vs. radial distance from HD 165052, shown separately for the eastward and westward directions. Symbols as in Fig. 20. Cyan, blue, and green, solid lines refer to normal distances of 1.82, 1.46, and 1.09 pc, respectively.

same observed effect. However, lacking these detailed geometrical informations on the nebula itself, we cannot derive better estimates, and may only consider $d_{\rm rad}$ = 1.09–1.46 pc as lower limits to the 9 Sgr distance from the part of the nebula immediately behind it.

This distance is much larger than the distance between the Orion-nebula ionizing star θ^1 Ori C and its molecular cloud, of ~0.25 pc (Wen & O'Dell 1995; O'Dell 2001). This difference is undoubtedly an important factor and may explain many of the differences we find between the properties of M 8 and the Orion nebula (see Sect. 3.4.1). It also suggests that 9 Sgr has excavated a larger cavity in its parent cloud compared to θ^1 Ori C, and in turn than the M 8 H_{II} region as a whole is probably in a later evolutionary stage than the Orion nebula.

Both Figs. 20 and 15a suggest that HD 165052 (O7Vz+O7.5Vz binary, Arias et al. 2002) is instead the dominant ionizing source in its neighborhood, despite being almost irrelevant to the nebular dynamics (Figs. 16 and 17). This is confirmed by the dependence of ionizing flux from distance to this star, shown in Fig. 21, analogous of Fig. 20; five arcmin to the west of HD 165052, the flux from 9 Sgr still dominates, but nearer to HD 165052 the 9 Sgr contribution becomes unimportant. We can therefore fit (although with higher uncertainties) a profile depending on the normal distance from HD 165052 to the cloud, as above: it turned out that also this star, like 9 Sgr, is likely to be found distinctly above the cloud, at a distance in the range 1.5–1.8 pc.

3.4. Position-velocity diagrams

3.4.1. The NGC 6530 region

Having discussed in Sect. 3.3 the existence of a reference direction for the nebular velocity field (arrow in Fig. 16), we study here position-velocity diagrams along this direction. This symmetry properties pertaining only to the region around the NGC 6530 cluster core, we consider here only the region (24 arcmin in diameter) within the red circle in Fig. 16. The relevant position-velocity diagram for Hα (with velocities from 1-g fits) is shown in Fig. 22. Positive projected distances are toward the arrow head of Fig. 16, that is toward the galactic plane (to N-W). The origin of distances is at the reference position of the NGC 6530 core, shown in Fig. 16. As mentioned, the low-mass cluster stars have a well-defined peak in their RV distribution, at $RV_{\rm cm}$ = 0.5 ± 0.2 km s^{-1} (Prisinzano et al. 2007); it is reasonable to assume that also the B stars in the same spatial region have the same mean RV. The most massive star in the cluster core region is HD 164906 (MWC280; type B0Ve, Levenhagen & Leister 2006). The cluster center coincides also with a CO bright spot (nr. 3 in Lada et al. 1976), at velocity $RV \sim +6$ km s^{-1} (heliocentric, corresponding to $v_{\rm LSR} \sim 16$ km s^{-1} as reported in Lada et al.), whose position is also shown in Fig. 17. As Fig. 22 shows, the cluster core corresponds to the expansion center, in both position and velocity, of a shell-like structure in the ionized gas, reaching maximum negative speeds of ~−12 km s^{-1}; no gas is found at $RV \sim RV_{\rm cm}$ in the vicinity of the cluster center. Interestingly, the colder CO molecular gas moves in the opposite direction with respect to $RV_{\rm cm}$, and Fig. 4 of Lada et al. (1976) also shows that it possesses a velocity gradient along the N-S direction, suggesting a shell-like geometry as well. The resulting picture is that of a localized expanding gaseous bubble, pushed by the cumulative effect of winds from massive B stars in the NGC 6530 cluster core (there are no O stars inside it). Therefore, in this part of the Lagoon nebula the nebular emission arises in front of the star cluster, not in its background. As the velocity map of Fig. 16 shows, such expansion is not spherical, with near-zero radial velocity reached at small distances only along the direction of the arrow. While dust extinction in front of the cluster stars is relatively low, it rises considerably behind them (e.g., Damiani et al. 2006), implying large amounts of dust just behind the cluster. Interestingly, there is no trace in Fig. 22 of any receding ionized shell, which we interpret with the ionizing radiation

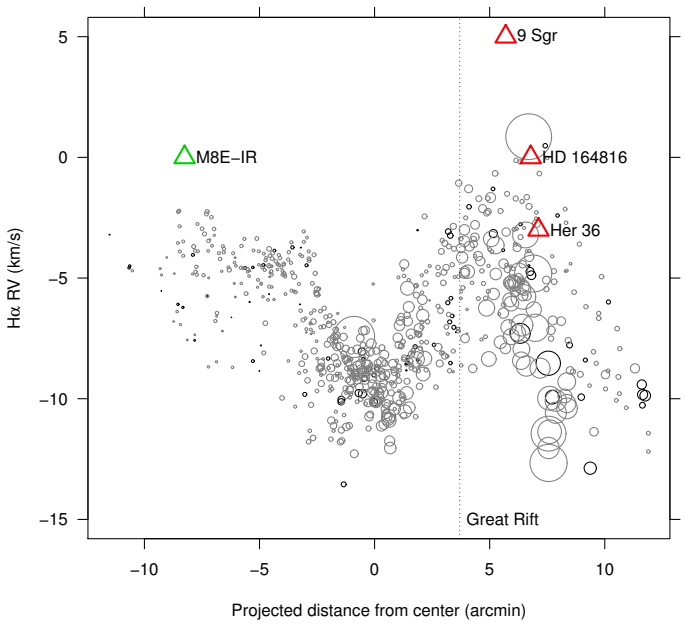

Fig. 22. Position-velocity diagram for Hα, inside the cluster core region (red dashed circle in Fig. 16). The projected distances in the abscissae are computed along the direction of the arrow also shown in Fig. 16. RVs from 1-g fits. Symbol size is proportional to line intensity from 1-g fits. Black (gray) circles refer to pure-sky (faint-star) fibres. The O star HD 164816 and the massive object M 8E-IR (triangles), for which no RV measurements are available, are plotted at $RV = 0$, that is the NGC 6530 cluster velocity, while the other triangles indicate massive-star RVs as reported in Table 1.

being absorbed by the dust on the rear side. For comparison, in the Orion nebula a rather regular sequence of velocities is found, with some of the ionized gas layers having speeds within a few km s^{-1} relative to the background CO ($\Delta RV \sim 3$ km s^{-1} for [S II], ~ 7 km s^{-1} for [O III], $\sim$10 km s^{-1} for Hα; O'Dell et al. 1993; O'Dell 2001). Here instead (and see also Fig. 26 below) we see little or no ionized gas at velocities so close to that of background CO, which points to important differences between the structure of the ionized regions in M 8 and in the Orion nebula. Also the emission from the PDR on the molecular cloud surface is not clearly recognizable in the position-velocity diagrams.

The stellar wind push of the massive stars in the NGC 6530 core, on the other hand, may be responsible for the peculiar positive-velocity displacement of the CO emitting gas (we note that the other two CO spots found by Lada et al. 1976, the brightest one coincident with the Hourglass nebula, have velocities $\sim$0 km s^{-1}, heliocentric). The current view that the star cluster did form on the near-side surface of the molecular cloud is in good agreement with the proposed interpretation: the far side of the star cluster faces regions with more dust, molecular gas, and higher-density gas in general, than the near side, facing the outer, more rarefied parts of the cloud. Therefore, also the absolute speed reached by the near-side ionized diffuse gas (~ -12 km s^{-1} in Hα) is larger than than of the far-side denser and colder gas ($\sim +6$ km s^{-1} in CO).

At projected distances larger than +5 arcmin, Fig. 22 shows a wide scatter in the RV distribution, with no clearly defined geometry; this region corresponds to the Hourglass nebula, as also clear from the size of the symbols in the figure (proportional to intensity). In the figure are also shown the massive stars M 8E-IR, HD 164816, 9 Sgr, and Herschel 36. Interpreting such a complex velocity field in term of expansion driven by one or more massive stars requires to know the radial velocity of these stars with sufficient accuracy. This information is not always available for massive stars, which have few lines broadened by very fast rotation, are found very often in binary systems, and are studied mostly with single-epoch observations. For convenience we compiled in Table 1 the literature radial-velocity data on the most massive stars discussed here, from the SIMBAD database, except for the 9 Sgr velocity taken from Williams et al. (2011); we note however that this star is a long-period SB2 binary, and the systemic velocity is subject to large errors (Rauw et al. 2012). No *Gaia*-ESO velocity measurements are available for these massive stars. Literature velocities are missing for four stars, including the massive young object M 8E-IR. These are plotted in our position-velocity diagrams at a velocity $RV_{\rm cm}$ for reference. The two stars in the western regions have similar velocities (~ -10 km s^{-1}), but strongly discrepant with $RV_{\rm cm}$; yet, they agree more with the approaching velocity of the Hα emission in the same region, discussed in Sect. 3.4.3 below. The positive velocity of 9 Sgr is surprising at first sight, being so different from that of the CO clouds; however, after considering that this star lies $\sim$1.5 pc above a massive molecular cloud ($2–6\times10^4$ $M_\odot$ for each of the CO clouds in the region according to Takeuchi et al. 2010, with the cloud associated with the Hourglass being one of the most massive), it becomes plausible that this star has gained a considerable speed toward the cloud during the last few Myrs.

From Fig. 22 there is no apparent connection between the position and motion of 9 Sgr and the ionized gas, despite this star being the most massive of the region. This supports further the arguments of Lada et al. (1976) on its lying at some distance from the cloud, in its foreground. In those outermost nebular regions, the local gas density is likely so low that the ionized front approaching us becomes undetectable. Outside the ionized regions, there is nevertheless neutral gas associated with the Lagoon nebula, as discussed in connection with sodium absorption in Sect. 3.2. Therefore, Fig. 23 shows the same Hα velocities as in Fig. 22, but on an expanded velocity scale, with the addition of the Na I D velocities: except for the dominant component near -5 km s^{-1}, the neutral gas moves at much larger negative velocities than the Hα-emitting gas. No clear pattern is seen, indicating that the geometry of the neutral-gas expansion is different from that of the ionized gas. It is interesting to remark that despite 9 Sgr is distant from the nebula, the sodium absorption is still closer to us, since several absorption components at negative velocities up to ~ -25 km s^{-1} or more are evident also in the 9 Sgr UVES spectra shown in Fig. 24. In this Figure a definite time variability of the sodium absorption components is seen, especially near velocities ~ -20 km s^{-1}, in both velocity and line width; this agrees with our arguments of Sect. 3.2 that the sodium layer at ~ -20 km s^{-1} is the one most subject to dynamical changes.

Consideration of the 2-g model fits to the Hα line in the same cluster core region provides us with only a marginally clearer picture (Fig. 25): the velocity splitting between blue and red components is here mostly small compared to the absolute velocity values. Again, near the shell center essentially no near-zero-velocity gas is detected, while maximum negative velocities attain ~ -15 km s^{-1}. In the Hourglass region the velocity spread is highest, again without clear geometrical pattern; we recall that this latter property agrees with the highly anisotropic brightness distribution of the Hourglass nebula itself, whose obscuring material lets the radiation from Herschel 36 leak only through irregularly-distributed windows.

Table 1. Literature data for massive stars in the Lagoon nebula.

Name	RA J2000	Dec J2000	Spectral type	RV km s^{-1}
HD 164536	270.6609	–24.2554	O7.5V	–10.5
7 Sgr	270.7129	–24.2825	F2/F3II/III	–11.1
Herschel 36	270.9180	–24.3785	O7:V	–3.0
9 Sgr	270.9685	–24.3607	O4V((f))z	5.0
HD 164816	270.9869	–24.3126	O9.5V+B0V	
HD 164865	271.0634	–24.1834	B9Iab	
M 8E-IR	271.2244	–24.4448		
HD 165052	271.2940	–24.3986	O7V+O7.5V	1.2
HD 165246	271.5195	–24.1955	O8V	

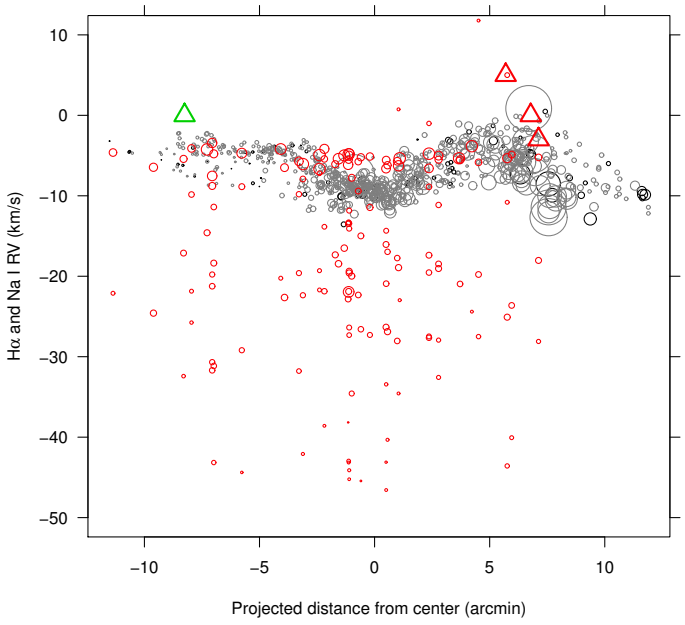

Fig. 23. The same diagram as in Fig. 22, but on a wider RV range to show also the Na I D2 absorption velocities (red circles).

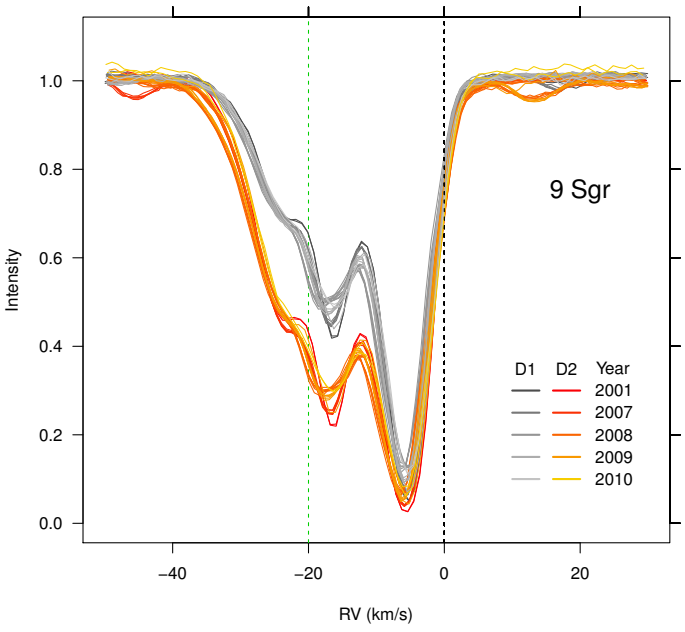

Fig. 24. Sodium doublet absorption toward 9 Sgr from UVES spectra between 2001–2010. Velocity $RV = -20$ km s^{-1}, where significant line-profile changes are found, is marked with a green dashed line.

More illuminating is the examination of the position-velocity diagram involving 2-g fits to [N II] and [O III] lines, and shown in Fig. 26. While the emission at velocities between 0 to −10 km s^{-1} has not greatly changed, new features are seen at both positive velocities (as in the map of Fig. 18b), and at velocities <−10 km s^{-1}. In the projected distance range from ∼−10 to ∼−3 arcmin a weak but significant positive-velocity component is found in both [N II] and [O III]. The velocity is found to be largest near the projected position of M 8E-IR (green triangle), and to decrease gradually toward position ∼−3 arcmin. There is no corresponding structure in the position-velocity plane at negative velocity. This suggests strongly the existence of a shell of ionized gas, expanding away from M 8E-IR (or its immediate vicinity), of which only the receding component is visible to us, and limitedly to the part unobscured by the dense bright-rimmed cloud. This latter characteristics is easily explained assuming that any approaching gas is blocked or hidden by the dark dusty structures seen as bright-rimmed clouds, which also occult M 8E-IR from our direct view. While all the literature on this object (see the review in Tothill et al. 2008) agrees that it must be very young and surrounded by thick layers of dust, the existence of a hemispheric shell ionized by this object implies that the dust thickness between M 8E-IR and the nebula behind it is much less than the dust thickness in the direction toward us. Alternatively, M 8E-IR, a known outflow source (Mitchell et al. 1991), might be only the source of the mechanical push exerted on the receding gas, which is instead ionized by another UV source, maybe 9 Sgr further away. Even in this latter case, the total column density of matter on our side of M 8E-IR must be much larger than on its rear side, in order to block any approaching gas expanding from it.

Considering now the region around 9 Sgr ($RV = +5$ km s^{-1}, Fig. 26), we observe that positive-velocity emission is found near its position, up to $RV \sim +12$ km s^{-1}, and declining away from the star position. Already in Fig. 18a the positive-velocity datapoints were seen to follow an almost half-arch around this star's position. While no (or very little) positive-velocity gas is found in correspondence of the cluster core, blocked by the dense molecular material behind, this blocking effect does not operate for the gas receding from 9 Sgr, if this star lies at large distances in front of the cluster as already discussed. Therefore, we obtain a coherent picture by assuming that the positive-velocity gas is pushed by 9 Sgr toward the nebula, counteracting its expansion locally.

The region around the Hourglass and Herschel 36 continues to show a rather chaotic position-velocity pattern even using the 2-g model fits in Fig. 26 as it was using 1-g models in Fig. 22 above. The largest green circle in Fig. 26 represents the strong negative-velocity [O III] emission in the Herschel 36 spectrum; a corresponding, much weaker positive-velocity component is also found near ∼+8.5 km s^{-1}, demonstrating again asymmetric expansion in the immediate vicinity of this star, where the high-ionization [O III] line arises.

Finally, Fig. 26 shows, in correspondence to cluster core, the largest negative velocities (up to ∼−25 km s^{-1}), which overlap with the velocities of the sodium absorption where indications of a hotter absorbing gas were found, as discussed in Sect. 3.2.

3.4.2. The Hourglass nebula

We next discuss position-velocity diagrams in the Hourglass region (defined as in Fig. 16); since the positive-velocity datapoints align along approximately the N-S direction in Fig. 18a, we take here the reference direction along RA for the position axis. The position-velocity diagram of Fig. 27 shows together

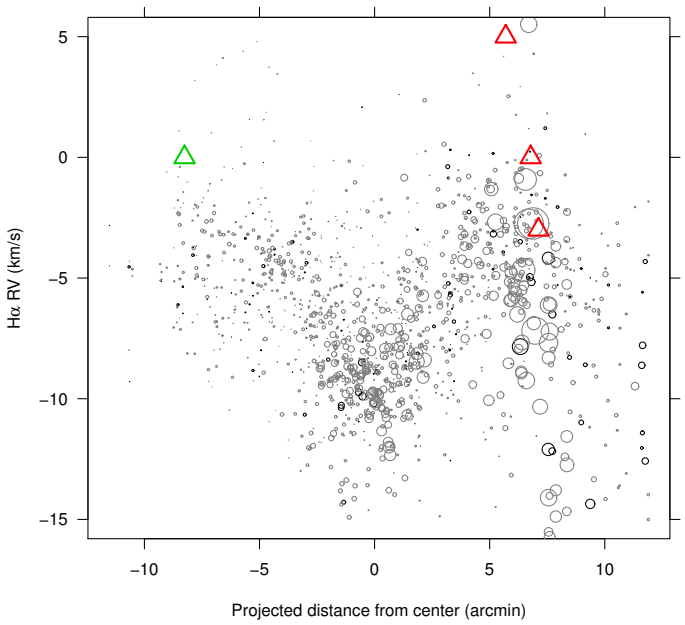

Fig. 25. Position-velocity diagram for Hα, cluster core, with RVs from 2-g fits. Symbol meaning as in Fig. 22.

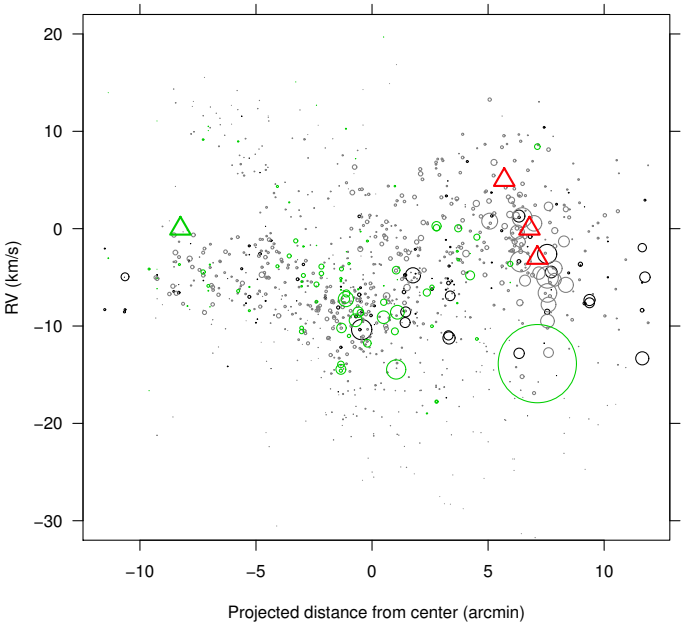

Fig. 26. Position-velocity diagram for [N II], cluster core, from 2-g fits. Also shown with green circles are the best-fit [O III] components.

the 2-g fit results from four lines: [N II], Hα, [O III], and Na I absorption. The position origin is taken coincident with the RA of 9 Sgr (RV = +5 km s^{-1}). Herschel 36 lies at RV = −3 km s^{-1}. The diagram, although very complex, helps us to appreciate better several effects. The [N II] emission, although found at both positive and negative velocities in the neighborhood of 9 Sgr, is on average stronger at positive RVs, whereas Hα is largely absent at positive RVs. This explains the discrepancy of bulk velocities between the two lines, found in Fig. 5a. To the right of position origin, the velocity splitting in Hα increases regularly until the position of Herschel 36: there, Hα shows both a negative-velocity component (reaching ∼−18 km s^{-1}), and a slower component, apparently at rest with respect to Herschel 36. On the other hand, [N II] shows both a rest-frame

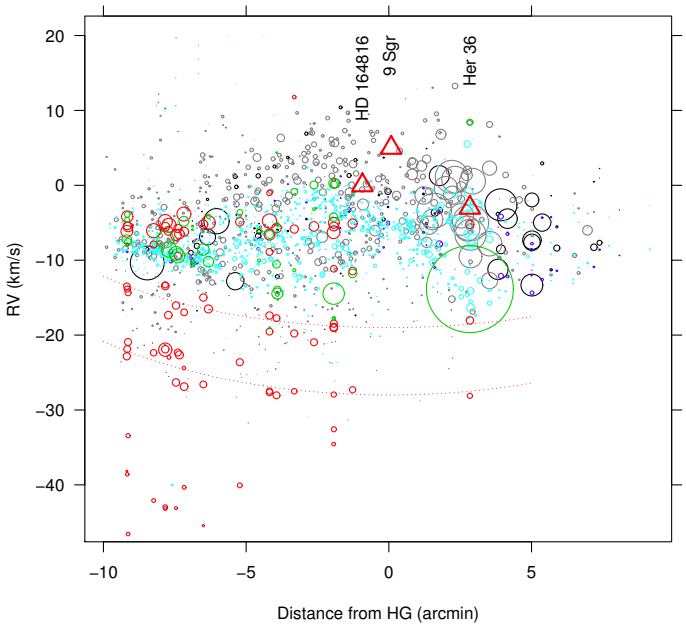

Fig. 27. Position-velocity diagram, in the Hourglass region (orange dashed circles in Fig. 16), showing RVs from 2-g fits. Circle size is proportional to line intensity. Positions in the abscissae are along RA direction, from the reference point shown in Fig. 16. Black and gray circles refer to [N II] (sky fibres and faint stars as in Fig. 22), blue and cyan circles refer to Hα, green circles to [O III], and red circles to Na I absorption. The large dotted circle segments are visually fit to the sodium datapoints.

component and another one with slightly receding velocities with respect to Herschel 36. Also in this case as for 9 Sgr, the Hα to [N II] intensity ratio is different between the near and far side of the massive star. We cannot make more quantitative studies since the intensity ratios for the (unresolved) 2-g fit components are affected by too large errors individually, as remarked in Sect. 3.1. The existence of positive-velocity [N II] emission from the envelope around Herschel 36, unlike the cluster core region, suggests that this star like 9 Sgr lies at some distance above the dust-rich molecular cloud, otherwise an inward-directed flow at positive velocities would have been blocked.

Much fainter than the positive-velocity [N II] emission, but still clearly detected is negative-velocity [N II] at ∼−20 km s^{-1}, overlapping some of the Na I absorption layers. As also discussed in Sect. 3.2, the transition between ionized and neutral gas should take place near this velocity range. Although the spatial coverage of the UVES data used for the study of the sodium line is much less dense than that of the Giraffe data, we may tentatively identify in the figure a regular pattern in the sodium absorption, as indicated by the two dotted red curves. These are centered to the 9 Sgr position, and suggest that the large-scale expansion, at distances where the gas is neutral, is driven by this star. The radii of the circle segments shown in Fig. 27 are respectively 13 and 15 arcmin, corresponding to 4.74 and 5.47 pc. The star 9 Sgr, showing sodium absorption at least around −20 km s^{-1}, must be interior to at least the lower-velocity shell, in agreement with its line-of-sight position derived in Sect. 3.3.2. By dividing the inferred sodium-shell radii by their maximum velocities we obtain timescales of order of 2–2.5 × 10^5 yr. Note however that even stars farther away from 9 Sgr than 15 arcmin show sodium absorption, so that the proposed geometry for the absorbing layers must be only considered as tentative, and more complex neutral-gas structures are

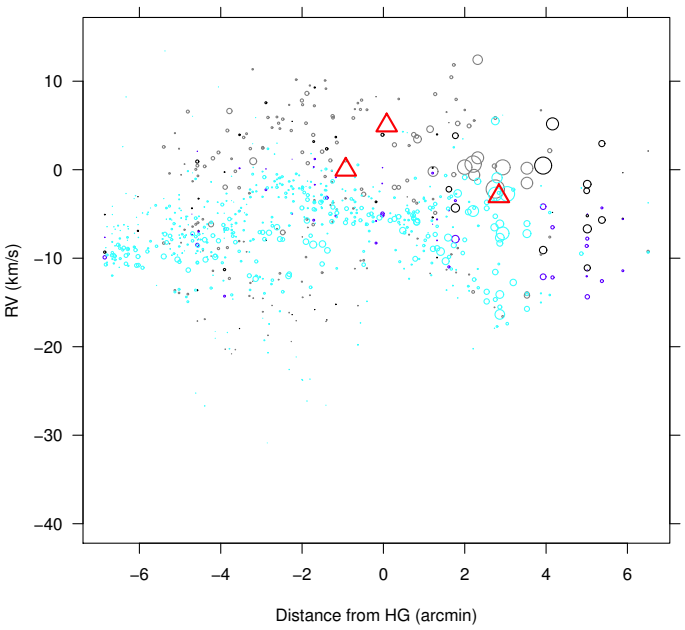

Fig. 28. Analogous of Fig. 27, but showing RVs from 2-g fits to [S II] (gray and black) and Hα (cyan and blue).

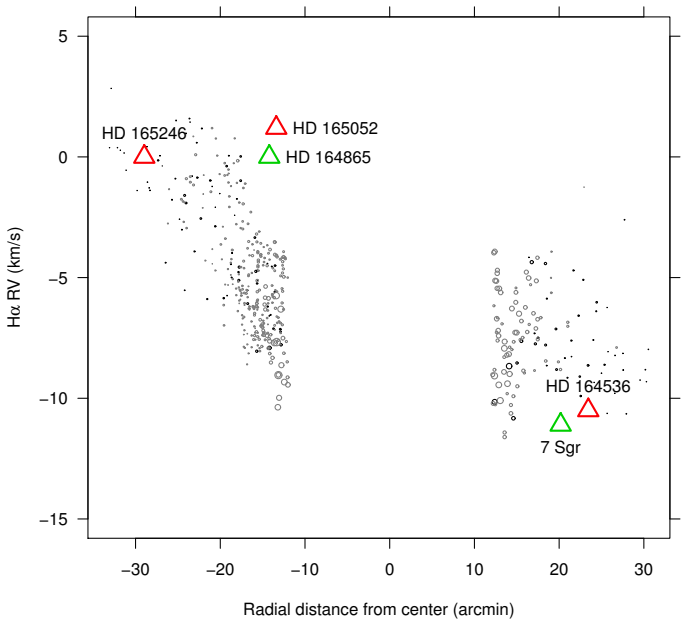

Fig. 29. Large-scale RV dependence on radius, from Hα (1-g fits). Only datapoints external to the cluster-core region (red dashed circle in Fig. 16) are shown. The abscissae show radial distances from cluster center (red plus sign in Fig. 16), shown separately for the eastern (left) and western (right) parts. Symbols as in Fig. 22.

certainly present across the entire face of the nebula. These layers, well above the ionized gas, and at negative velocities with respect to it, are very similar to the Orion Veil, already mentioned in Sect. 3.1. The existence of a blueshifted, neutral layer is also in very good agreement with predictions of champagne-flow models of blister H_{II} regions (Tenorio-Tagle 1979), fully appropriate to a region like M 8.

The results from the 2-g fits to [S II] lines, shown in Fig. 28, provide independent confirmations of the findings just discussed. In particular the brightest [S II] emission near Herschel 36 is found near the stellar rest velocity (as for Hα), but clear [S II] emission near the Hourglass is found also at positive velocities (while Hα shows large negative velocities in the same region).

3.4.3. The outer parts of the Lagoon nebula

Finally, we examined the large-scale velocity patterns of the nebula, outside the central parts examined above. We have already remarked that the western regions do not show the same dynamics as the eastern ones, and therefore a radial coordinate does not prove useful. Instead, we consider separately an east and a west radial coordinate, from the same NGC 6530 cluster center as in Sect. 3.4.1. The dependence of 1-g Hα velocity on these radial distances is shown in Fig. 29. Toward east the gradual decrease in absolute velocity (toward RV_{cm}) agrees well with a global-expansion pattern, with velocity vectors becoming orthogonal to the line of sight at the largest radii. To the west, there is no sign of this, with velocities remaining at values from -10 to -5 km s^{-1} even where the nebula becomes very faint. Our spatial sampling in the S-W outer regions is almost nonexistent, so these result pertain essentially to the N-W parts, that is those closest to the galactic plane. Adding complexity to the puzzle, the two massive stars in the west (HD 164536 and 7 Sgr) both have negative velocities, similar to the neighboring gas but contrasting with RV_{cm}.

One possible explanation of the east-west large-scale velocity gradient in the Lagoon is rotation. In order to keep in bound keplerian rotation matter at a speed of 5 km s^{-1} at a radius of 10-11 pc, and in the absence of internal pressure support, a mass of 6×10^4 $M_\odot$ is required, which is not unreasonable compared to the mass estimates for the CO clouds in M 8 given by Takeuchi et al. (2010) using NANTEN, or the value of 10^4 $M_\odot$ given for the M 8-East region alone by Tothill et al. (2008). However, one obvious difficulty of this hypothesis is that, if this was the case, then Fig. 29 would suggest for the cloud center of mass a $RV \sim -5$ km s^{-1}, in strong disagreement with the RVs of both the CO bright spots of Lada et al. (1976) and the NGC 6530 RV_{cm}.

The adoption of 2-g fits does not clarify the issue of large-scale dynamics, even using [N II] and [O III] having smaller linewidths (Fig. 30): not only the datapoint scatter is increased, but the overall east-west velocity gradient becomes barely observable in these lines, which therefore originate in layers well distinct from Hα. For some locations, as discussed in Sect. 3.3.1, the [N II] lines are split, with central RV very close to that of the nearby O star HD 164536: these add to the scatter seen in the rightmost datapoints in Fig. 30, where local expansion adds to the average local cloud velocity. The splitting center being so close to the O-star RV might also be seen as a confirmation that the (poorly studied) star HD 164536 lies within the Lagoon itself. The figure also shows velocities of sodium absorption components, which may be of some usefulness: if we consider the lowest-found (absolute) sodium velocities at various radial distances, we may observe a regular gradient from $RV \sim 0$ km s^{-1} at the east extreme, toward $RV \sim -5$ km s^{-1} at the opposite one. As discussed in Sect. 3.2, this sodium layer, being the most uniform of all found here, is probably the outermost one, and therefore least affected by local phenomena. If it is really associated with the Lagoon nebula, it might be considered as the best indicator of a global rotation of the nebula. A much better spatial coverage in the sodium absorption data would be needed, however, before accepting this possibility.

Alternatively, the observed velocity gradient might reflect a shear motion, caused by interaction between the parts of M 8

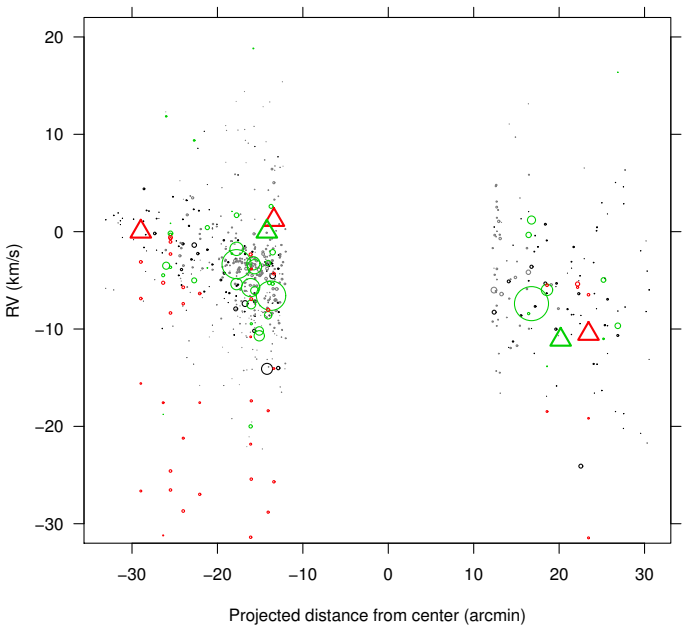

Fig. 30. Same as Fig. 29, but showing RVs from 2-g fits to [N II] (black and gray) and [O III] (green). Also shown are RVs of Na I absorption (red).

closest to the galactic plane (to the northwest) and other dense clouds.

4. Discussion and summary

The various pieces of evidence described in Sect. 3 enable us to draw a complex picture of the ionized and neutral gas in the Lagoon nebula, and of its physical connection to massive stars and molecular material in the cloud. Perhaps the most effective way of building a coherent and understandable picture is by means of a drawing. We show therefore a graphical summary of most of the results obtained in Fig. 31, which refers to a section through the nebula along a line joining M 8E-IR with the Hourglass region, until the western nebula parts. The figure represents most of our findings with some level of detail. It shows the approximate boundary of the molecular cloud, dusty regions, and some O stars as a reference.

The core of the NGC 6530 cluster is shown, where most of its B stars are found; the entire cluster would fill most of the region shown. The B stars drive a strong expanding shell toward us visible in the ionized-gas lines. On the opposite (far) side of the cluster, no redshifted expansion is detected in the ionized lines, suggesting that the cluster lies very close to the denser, dusty molecular cloud, as shown. The CO clump in the same direction is redshifted (Lada et al. 1976; Takeuchi et al. 2010), probably pushed by the same cluster stars producing the blueshifted optical lines. We represent this with the magenta dashed arcs. Note that the other two strong CO clumps in this region (also labeled "CO" in the figure) are found at rest with respect to the NGC 6530 $RV_{\rm cm}$.

The Hourglass region around Herschel 36 lies probably at some distance from the background molecular cloud, since some high-velocity redshifted emission is seen around it, as well as blueshifted emission. The geometry of any material expanding away from Herschel 36 is however very irregular, because of the non-isotropic distribution of dense clouds all around this star: we represent this as discontinuous shell fragments, both redshifted and blueshifted. We recall that the nebular densities found in this region are the highest of the whole Lagoon nebula.

The M 8-East region is also characterized by a partial-shell geometry, since we detect the unobscured portion of a redshifted expanding arc, centered on M 8E-IR. This star, or another sufficiently massive star near to it, must be heavily obscured on our side (tens of magnitudes visually), but very little on the inner side, in order to be able to drive an inward flow. The outward flow is instead blocked by the dense cloud, and its blueshifted emission not detected accordingly.

A crucial role is played by the most massive star, 9 Sgr, which we find to lie well separated (at least 1 pc, or more) from the cloud surface, in agreement with previous works, but still inside the large blister concavity. Being found in a low-density environment, its radiative and mechanical push becomes detectable only against the higher-density gas on the inward side of the star, as redshifted emission in [N II] and [S II]; on its outward side, very faint or undetectable blueshifted emission is present. A combination of factors may therefore explain the characteristics found in the Great Rift region: it is denser than its surroundings, being compressed by both sides (NGC 6530 shell and Herschel 36 shell), and pushed toward the cloud by the 9 Sgr wind and radiation, hence the positive velocities on its ionized surface. It would be interesting to examine whether such compression is able to trigger new star formation. There is no contradiction between the enhanced dust density in the Great Rift, responsible for obscuration of background stars, and the inconspicuous electron density found there from the [S II] doublet ratio (Fig. 15b), since this latter only refers to its ionized surface and not to its colder, inner parts.

Completing the picture, the western parts of the cloud are found to be approaching us, as is the O star HD 164536, whose wind is probably responsible of some line splitting in its vicinity, indicative of a bidirectional expansion, as shown. At large distances in front of the whole cloud, discrete neutral layers are found, approaching us over a range of (negative) velocities and distances. They might be named the "Lagoon Veil", by analogy with the Orion Veil.

In addition to these results, at least another one deserves some discussion. The velocity profile around NGC 6530, whatever the diagnostic line and the modeling approach (1-g or 2-g) chosen, leaves little doubt about an expanding shell being driven by stars in the cluster core. At the same time, both the ionization parameter (Fig. 15a) and the ionizing flux (Fig. 20) show a gradient across the cluster face, in the direction of 9 Sgr. The latter figure shows that, with respect to the 9 Sgr ionizing flux, only a small excess (less than a factor of 2) is found at the NGC 6530 position, attributable to the NGC 6530 B stars themselves. Therefore we reach the conclusion, on solid observational grounds, that the NGC 6530 shell is mechanically driven from inside, but ionized from outside. This geometry is very unlike classical Strömgren spheres. A deeper treatment of the problem is clearly outside our scopes here. The biggest problem is, since we observe recombination in the Hα line, where the recombined neutral gas lies: gas outside of the shell is ionized by 9 Sgr, inside it is ionized by the NGC 6530 B stars. Perhaps a double shell develops, with an intermediate sheet of neutral gas: this might account for the small velocity splitting indicated by our 2-g fits to Hα lines. In the absence of a detailed modeling, we cannot however derive any firm conclusion on this issue.

Another interesting issue is that related to rotation of the entire cloud, as suggested by the blueshifted lines in the N-W parts. It is worth noting in this respect that in the molecular CO lines the appearance of the Lagoon nebula is very different than in

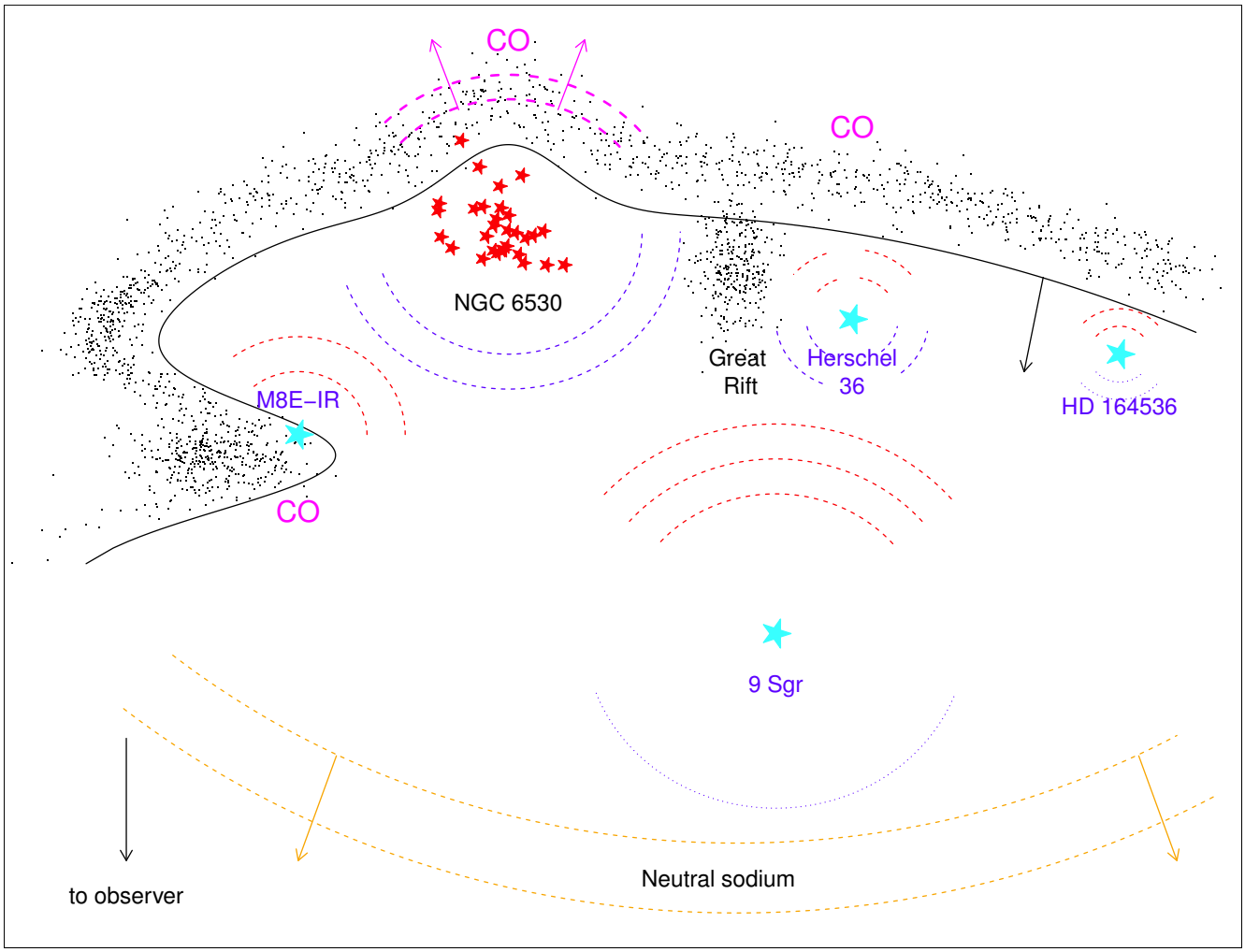

Fig. 31. Schematic representation of the Lagoon nebula geometry, along a direction passing through M 8E-IR and the Hourglass nebula. The black line indicates the molecular cloud boundary. Dusty regions are indicated with dots. Red (blue) dashed arcs indicate redshifted (blueshifted) ionized gas. Triple arcs indicate more conspicuous emission, single arcs weak emission; broken arcs indicate irregular shells. The position and motion of the known CO clouds is indicated in magenta. The most massive stars and the NGC 6530 cluster core are indicated with cyan and red stars respectively. The large-scale sodium layers are also shown (yellow dashed lines), probably not to scale.

the optical, and splits in three main condensations, coincident with M 8-East, NGC 6530 core, and Hourglass regions respectively, with little in between (Fig. 8 of Takeuchi et al. 2010). The Lagoon N-W regions appear as an extension of the Hourglass CO cloud, whose core is at rest with respect to $RV_{\rm cm}$. It is therefore possible that only the Hourglass molecular cloud is rotating, not the entire Lagoon nebula; this motion does not involve NGC 6530 and is in better agreement with the other existing dynamical data. Alternatively, the CO maps of Takeuchi et al. (2010) make it clear that the N-W region, the closest to the galactic plane, is also near other CO clouds, and might be interacting with them. Therefore, while the bulk motion of approach of the N-W Lagoon nebula region is an established observational result, its interpretation is not unambiguous.

Acknowledgements. We wish to thank an anonymous referee for his/her many interesting comments and suggestions. Based on data products from observations made with ESO Telescopes at the La Silla Paranal Observatory under program ID 188.B-3002. These data products have been processed by the Cambridge Astronomy Survey Unit (CASU) at the Institute of Astronomy, University of Cambridge, and by the FLAMES-UVES reduction team at INAF-Osservatorio Astrofisico di Arcetri. These data have been obtained from the *Gaia*-ESO Survey Data Archive, prepared and hosted by the Wide Field Astronomy Unit, Institute for Astronomy, University of Edinburgh, which is funded by the UK Science and Technology Facilities Council. This work was partly supported by the European Union FP7 program through ERC grant number 320360 and by the Leverhulme Trust through grant RPG-2012-541. We acknowledge the support from INAF and Ministero dell' Istruzione, dell' Università' e della Ricerca (MIUR) in the form of the grant "Premiale VLT 2012". T.Z. acknowledges support from the Slovenian Research Agency (research core funding No. P1-0188). F.J.-E. acknowledges financial support from the Spacetec-CM project (S2013/ICE-2822). M.T.C. acknowledges the financial support from the Spanish Ministerio de Economía y Competitividad, through grant AYA2016-75931-C2-1-P. The results presented here benefit from discussions held during the *Gaia*-ESO workshops and conferences supported by the ESF (European Science Foundation) through the GREAT Research Network Programme. This work is also based on data products from observations made with ESO Telescopes at the La Silla Paranal Observatory under program ID 177.D-3023, as part of the VST Photometric Hα Survey of the Southern Galactic Plane and Bulge (VPHAS+, www.vphas.eu). This research has made use of the SIMBAD database, operated at CDS, Strasbourg, France.

References

Arias, J. I., Morrell, N. I., Barbá, R. H., et al. 2002, MNRAS, 333, 202
Bagnulo, S., Jehin, E., Ledoux, C., et al. 2003, The Messenger, 114, 10
Balick, B., Gammon, R. H., & Hjellming, R. M. 1974, PASP, 86, 616
Bohuski, T. J. 1973, ApJ, 184, 93
Brand, P. W. J. L., & Zealey, W. J. 1978, A&A, 63, 345
Damiani, F., Flaccomio, E., Micela, G., et al. 2004, ApJ, 608, 781
Damiani, F., Prisinzano, L., Micela, G., & Sciortino, S. 2006, A&A, 459, 477
Damiani, F., Bonito, R., Magrini, L., et al. 2016, A&A, 591, A74

Drew, J. E., Gonzalez-Solares, E., Greimel, R., et al. 2014, MNRAS, 440, 2036
Elliott, K. H., & Meaburn, J. 1975, MNRAS, 172, 427
Gilmore, G., Randich, S., Asplund, M., et al. 2012, The Messenger, 147, 25
Henning, T., & Gürtler, J. 1986, Ap&SS, 128, 199
Hobbs, L. M. 1974, ApJ, 191, 381
Kaufman, U., & Martin, W. C. 1993, J. Phys. Conf. Ser., 22, 279
Kramida, A., Ralchenko, Yu., Reader, J., & NIST ASD Team 2015, NIST Atomic Spectra Database (v. 5.3), http://physics.nist.gov/asd
Kumar, D. L., & Anandarao, B. G. 2010, MNRAS, 407, 1170
Lada, C. J., Gottlieb, C. A., Gottlieb, E. W., & Gull, T. R. 1976, ApJ, 203, 159
Levenhagen, R. S., & Leister, N. V. 2006, MNRAS, 371, 252
Meaburn, J. 1971, Ap&SS, 13, 110
Mitchell, G. F., Maillard, J.-P., & Hasegawa, T. I. 1991, ApJ, 371, 342
Munari, U., & Zwitter, T. 1997, A&A, 318, 269
O'dell, C. R. 2001, ARA&A, 39, 99
O'dell, C. R., Valk, J. H., Wen, Z., & Meyer, D. M. 1993, ApJ, 403, 678
O'Dell, C. R., Muench, A., Smith, N., & Zapata, L. 2008, Handbook of Star Forming Regions, Vol. I, ed. B. Reipurth (ASP Monograph Publications), 4, 544
Pasquini, L., Avila, G., Blecha, A., et al. 2002, The Messenger, 110, 1
Povich, M. S., Kuhn, M. A., Getman, K. V., et al. 2013, ApJS, 209, 31
Prisinzano, L., Damiani, F., Micela, G., & Sciortino, S. 2005, A&A, 430, 941
Prisinzano, L., Damiani, F., Micela, G., & Pillitteri, I. 2007, A&A, 462, 123
Randich, S., Gilmore, G., & Gaia-ESO Consortium 2013, The Messenger, 154, 47
Rauw, G., Sana, H., Spano, M., et al. 2012, A&A, 542, A95
Saraph, H. E., & Seaton, M. J. 1970, MNRAS, 148, 367
Simon, M., Cassar, L., Felli, M., et al. 1984, ApJ, 278, 170
Sung, H., Chun, M.-Y., & Bessell, M. S. 2000, AJ, 120, 333
Takeuchi, T., Yamamoto, H., Torii, K., et al. 2010, PASJ, 62, 557
Tenorio-Tagle, G. 1979, A&A, 71, 59
Tothill, N. F. H., White, G. J., Matthews, H. E., et al. 2002, ApJ, 580, 285
Tothill, N. F. H., Gagné, M., Stecklum, B., & Kenworthy, M. A. 2008, Handbook of Star Forming Regions, Vol. II, ed. B. Reipurth (ASP Monograph Publications), 5, 533
van den Ancker, M. E., The, P. S., Feinstein, A., et al. 1997, A&AS, 123, 63
Viironen, K., Delgado-Inglada, G., Mampaso, A., Magrini, L., & Corradi, R. L. M. 2007, MNRAS, 381, 1719
Walker, M. F. 1957, ApJ, 125, 636
Weedman, D. W. 1968, PASP, 80, 314
Welsh, B. Y. 1983, MNRAS, 204, 1203
Wen, Z., & O'dell, C. R. 1995, ApJ, 438, 784
Williams, S. J., Gies, D. R., Hillwig, T. C., McSwain, M. V., & Huang, W. 2011, AJ, 142, 146
Woodward, C. E., Pipher, J. L., Helfer, H. L., et al. 1986, AJ, 91, 870
Wright, E. L., Lada, C. J., Fazio, G. G., Low, F. J., & Kleinmann, D. E. 1977, AJ, 82, 132

Appendix A: Additional tables

Table A.1. Fitting results (1-g models) for nebular emission lines.

Id	RA	Dec	Hα			[N II] 6584			[S II] 6717			[S II] 6731		
	(J2000)		RV	σ	Norm	RV	σ	Norm	RV	σ	Norm	RV	σ	Norm
SKY_18041349-2406277	271.0562	-24.10769	–4.44	13.33	13604.47	–3.32	9.82	5303.02	–2.45	9.49	893.61	–2.19	9.48	653.69
SKY_18040836-2411076	271.0348	–24.18544	–8.67	13.35	71283.37	–5.89	13.05	10866.23	–3.70	12.88	2182.28	–3.58	12.71	1608.08
SKY_18041039-2413163	271.0433	–24.22119	–2.41	13.35	44833.48	2.03	10.90	6861.96	2.98	10.89	1360.72	2.84	10.59	997.84
SKY_18043822-2413504	271.1592	–24.23067	–7.78	14.11	32206.53	–4.93	11.19	6559.79	–4.35	11.04	1178.57	–4.06	10.83	856.31
SKY_18043552-2406457	271.1480	–24.11269	–5.75	13.88	8302.00	–4.48	10.82	3030.67	–4.37	10.60	661.15	–4.14	10.58	478.39
SKY_18043039-2411382	271.1266	–24.19394	–7.91	13.73	45666.66	–4.08	11.60	10108.42	–2.68	11.34	1992.34	–2.49	11.19	1479.74
SKY_18044986-2410494	271.2077	–24.18039	–6.08	13.54	24539.49	–3.82	11.38	8360.59	–1.76	11.49	1839.73	–1.83	11.10	1320.87
SKY_18042865-2415336	271.1194	–24.25933	–8.52	13.18	44827.42	–5.82	10.46	7341.40	–4.70	10.00	1366.45	–4.62	9.83	1034.42
SKY_18043273-2417261	271.1364	–24.29058	–8.83	13.68	16638.05	–4.96	11.79	2305.00	–4.53	11.39	531.72	–4.47	10.64	388.39
SKY_18045577-2415459	271.2324	–24.26275	–7.12	14.10	21283.13	–4.00	12.58	6772.99	–4.41	12.38	1149.48	–4.32	12.05	821.87
SKY_18043471-2416492	271.1446	–24.28033	–8.51	13.62	46025.05	–5.27	11.36	5759.30	–3.64	11.00	1221.82	–3.59	10.72	925.07
SKY_18050209-2410250	271.2587	–24.17361	–5.00	14.01	11658.67	–3.08	11.63	4058.60	–2.10	11.18	937.26	–1.71	11.51	690.53
SKY_18050407-2417194	271.2670	–24.28872	–6.59	14.11	6440.37	–5.05	11.84	1703.00	–4.56	11.63	396.81	–4.29	11.64	290.20
SKY_18043741-2418209	271.1559	–24.30581	–9.02	14.09	53120.50	–7.15	12.93	7183.70	–5.76	12.30	1375.30	–5.75	11.92	1008.91
SKY_18042325-2423135	271.0969	–24.38708	–9.76	13.04	92195.82	–9.26	12.77	10544.73	–6.68	12.47	2340.38	–6.23	12.22	1782.30
SKY_18042233-2424399	271.0930	–24.41108	–10.13	13.35	81644.76	–9.24	12.86	12434.13	–8.79	12.66	2410.94	–8.44	12.43	1806.04
SKY_18035290-2419527	270.9704	–24.33131	–4.73	13.29	103114.41	–0.16	11.45	15344.15	1.19	11.42	2948.04	1.59	11.08	2451.45
SKY_18040022-2416517	271.0009	–24.28103	0.48	14.22	58118.20	8.01	12.99	7824.35	6.78	14.20	1210.24	6.85	13.96	917.58
SKY_18034573-2418216	270.9405	–24.30600	–9.93	13.65	84000.85	–3.75	10.69	18035.57	–2.44	10.97	3429.26	–2.19	10.65	2984.15
SKY_18030577-2416564	270.7740	–24.28233	–7.74	13.96	27976.36	–6.61	11.41	8938.61	–6.18	11.04	1992.20	–5.86	11.16	1526.26

Notes. Units of RV and σ columns are km s^{-1}. Units of Norm columns are ADU km/sec/min. Full table available at the CDS.

Table A.2. Fitting results for Na I D2 lines.

Id	Name	v_1 (km s^{-1})	σ_1 (km s^{-1})	N_1 (km s^{-1})	v_2 (km s^{-1})	σ_2 (km s^{-1})	N_2 (km s^{-1})	v_3 (km s^{-1})	σ_3 (km s^{-1})	N_3 (km s^{-1})	v_4 (km s^{-1})	σ_4 (km s^{-1})	N_4 (km s^{-1})	v_5 (km s^{-1})	σ_5 (km s^{-1})	N_5 (km s^{-1})
580-1	18040126-2423474	–5.01	1.48	208.52	–11.14	10.10	6.69	–18.47	2.20	10.29	–27.94	5.63	2.13			
580-2	18041116-2421452	–1.01	8.68	2.66	–4.77	1.23	3071.49	–17.38	3.36	11.62	–27.48	3.75	4.28			
580-3	18042056-2424556	–4.98	1.13	2029.78	–16.51	7.44	20.68									
580-4	18042433-2415168	–3.84	1.01	2523.49	–24.40	2.57	0.55									
580-5	18042502-2427453	–6.50	3.00	80.45	–22.64	4.72	21.36									
580-6	18042663-2419321	–5.34	1.12	2811.36	–22.97	1.52	0.66									
580-7	18042720-2422497	–4.84	1.06	2667.80	–13.44	7.88	14.49	–21.95	0.57	1435.09	–43.16	1.04	0.55			
580-8	18043893-2424142	–4.19	1.27	1458.15	–20.24	3.10	1.66									
580-9	18044279-2418339	–4.75	1.26	455.51	–14.07	3.00	5.41	–19.38	1.73	12.75	–26.37	2.66	4.45	–45.23	3.00	0.48
580-10	18044593-2427191	–4.24	1.24	3100.19	–14.59	8.59	13.68									
580-11	18045062-2425419	–3.43	1.46	338.62	–8.78	3.19	35.49	–21.24	9.12	8.65	–30.68	1.26	6.12			
580-12	18045273-2417525	–4.94	1.14	2850.68	–19.30	3.54	1.74									
580-14	18053923-2407522	–5.25	1.75	157.38	–17.57	3.92	4.92	–31.20	2.53	0.52						
580-16	18055648-2416004	–0.59	2.72	965.69	–0.74	7.46	27.64	–24.58	2.41	35.00	–41.33	0.21	0.14			
520-1	18023863-2415195	–6.48	2.33	27.77	–19.17	2.70	2.83	–31.45	3.79	6.19						
520-2	18024192-2433360	–5.38	1.03	2573.53	–5.72	3.00	12.44									
520-3	18025328-2420170	–5.50	2.11	38.28	–18.47	4.37	5.14	–33.29	2.22	4.39						
520-4	18033016-2430506	–5.33	0.97	2438.88	–5.58	3.00	13.45									
520-5	18034033-2422427	–5.23	2.98	24.67	–18.03	5.00	12.82	–28.11	5.00	2.10						
520-6	18035837-2429128	–5.12	1.61	54.09	–11.45	4.54	16.17	–27.30	3.87	4.89						

Notes. Column Id is the Setup+star identifier used in Sect. 3.2. Column Name is based on J2000 star coordinates. Units of N_i are the same as σ_i by Eq. (3). Full table available at the CDS.